Force Sensitivity of the Von Willebrand Factor A2 Domain

Professor Timothy Springer Amy Jia Xu

Force Sensitivity of the von Willebrand Factor A2 Domain

Abstract

von Willebrand factor (VWF) is a multimeric glycoprotein that critically supports platelet aggregation in hemostasis. Disordered VWF function causes both thrombotic and bleeding disorders, and genetic defects in VWF are responsible for von Willebrand's disease (VWD), the most common inherited bleeding disorder in humans. Very large VWF multimers exhibit the greatest thrombogenic activity, which is attenuated by ADAMTS13 cleavage in the A2 domain. A2 cleavage is regulated by mechanical force, and pathologically high shear forces are known to enhance proteolysis and cause bleeding in patients. Enhanced cleavage is also described in patients with VWD 2A mutations. In contrast, VWF A2 is stabilized against cleavage by a calcium binding site within A2. Single molecule studies have demonstrated that mechanical unfolding is required for A2 cleavage to expose the scissile bond. In this dissertation, we aim to better understand the mechanosensitivity of A2 cleavage by characterizing the force sensitivity of A2 unfolding and refolding.

We first characterized the interaction between VWF A2 and calcium using bulk isothermal calorimetry and thermal denaturation assays. In parallel, we used single molecule optical tweezers to characterize A2 unfolding and refolding. Calcium was found to bind A2 with high affinity, stabilize A2 against thermal denaturation, and enhance domain refolding. In contrast, we found that VWD 2A mutations destabilize the A2 domain against thermal denaturation. R1597W, the most common VWD 2A mutation, lies within the calcium binding loop and exhibited diminished calcium stabilization against thermal denaturation. Using optical tweezers, we found that R1597W also diminished A2 refolding. R1597W refolding in the presence of calcium was similar to that of wild-type A2 in the absence of calcium, suggesting that loss of calcium stabilization contributes to the disease mechanism of R1597W. Other VWD 2A mutations lying outside the calcium binding loop also destabilized A2, but retained

calcium mediated stabilization. These studies provide a better understanding of VWD 2A pathophysiology and offer structural insights into A2 unfolding and refolding pathways. By exploring the role of mechanical force in regulating VWF cleavage, this work moves towards a better understanding of how hydrodynamic forces within the vasculature regulate VWF function in hemostasis and thrombosis.

Table of Contents

Acknowledgements

I am forever indebted to the rigorous guidance and expectations of my thesis advisor, Timothy Springer, who inspires me to probe deeply, think quantitatively and reach across disciplines. I admire his remarkable patience in training me, and his ability to encourage progress by approaching obstacles with tenacious curiosity. It has been a great privilege to work on a thesis topic I have found so fascinating, and it will be my lifelong quest to emulate Tim's creative brilliance, dedicated diligence, and scientific passion. I am also grateful for the warm kindness of Chafen Lu, whose invaluable expertise cultivates the productive laboratory environment I have been fortunate to benefit from. My training in the Springer lab has instilled in me an appreciation for structural mechanisms that I will carry throughout my future endeavors in science and medicine.

The Springer lab has been an incredible environment for me to train in, and I have been privileged to benefit from the expertise of all members of the lab. In particular, I thank Frank Zhang for supervising me during my initial rotation in the lab, Jieqing Zhu for his insightful guidance for protein expression, and Jongseong Kim and Chenzhong Zhang for their camaraderie and expertise while building our Optical Tweezers machine together. I have learned a lot from working with everyone in the lab and am grateful for the lab's knowledge and generosity.

I thank Steve Blacklow for mentoring my personal and scientific development, and for directing a vibrant MD/PhD program I am humbled to be a part of. Jim Hogle and Michele Jakoulov run an incredible Biophysics PhD program, and I thank them for their dedication and heart in supporting every step of my graduate studies.

I appreciate the support of my Dissertation Advisory Committee, David Golan, Steve Blacklow, and Wesley Wong, and especially thank David Golan, Steve Blacklow, and Jim Hogle for serving double duty on my examining committee as well. Their thoughtful contributions and commitment to my training are deeply appreciated.

Finally, I would like to thank my late father, Jingchun Xu, younger sister, Maria Xu, and mother, Pingnian He, for cultivating my love of learning and always believing in me. I cherish my incredible family for enriching my life with love and laughter, and know we will always be together in spirit. From my father's battle with thymoma, to my sister's never-ending optimism, to my mother's achievements as a tenured professor and single mother, their resilience inspires my humanity and I cannot imagine more powerful relationships to draw strength from. I deeply appreciate this privilege to train at Harvard Medical School in the Medical Scientist Training Program and look forward to a career stimulated by curiosity, compassion, and profound meaning.

Chapter I:

Biophysics of VWF in Hemostasis and Thrombosis

Amy J. Xu and Timothy A. Springer

Introduction

von Willebrand factor (VWF) is an adhesive glycoprotein that critically mediates hemostasis by supporting platelet aggregation and stabilizing factor VIII. Disordered VWF function is implicated in both thrombotic and bleeding disorders, and genetic defects in VWF are responsible for the most commonly inherited bleeding disorder in humans. Secreted into the circulation as enormous concatamers, VWF experiences significant hydrodynamic forces that regulate its function. Above a critical shear rate, VWF transitions from globular to elongated conformations, which activate its adhesive function. These conformational dynamics are dictated by shear gradients that result in elongational flows. Elongational flows are enhanced in both hemostasis and thrombosis through changes in vessel geometry. Mechanical force also regulates VWF proteolysis by ADAMTS13, which determines the size, and thus thrombogenicity, of VWF multimers. VWF and platelets interact through a structural bond that is remarkably specialized for arteriolar flow to remain stable under high shear. These specialized interactions can be studied through single molecule experiments to gain insight into the structural specializations of VWF domains that enable force sensitive cleavage and force resistant platelet binding. The following review discusses how VWF function is regulated by shear, the hydrodynamic forces experienced by VWF, and the structural features of individual domains that render VWF sensitive to mechanical force.

VWF critically mediates hemostasis

von Willebrand factor (VWF) is a large, multimeric glycoprotein central to hemostasis. At sites of vascular injury, several mechanisms function to arrest bleeding. First, damaged blood vessels constrict to reduce blood flow, increase shear, and create a shear grdient. Next, platelets aggregate to plug the vessel defect. Finally, the coagulation cascade stabilizes the initial platelet plug through fibrin cross-linking. The structure of VWF highlights its critical function in these hemostatic mechanisms, as different domains bind collagen, platelet glycoprotein Ib (GPIb), integrins $\alpha_{IIb}\beta_3$ and $\alpha_V\beta_3$, and clotting factor VIII (Fig 1.1A). VWF mediates platelet plug formation by binding platelets and anchoring to the vessel wall through interactions with $\alpha_V\beta_3$ integrins on endothelial cells (1) and collagen exposed within the sub-endothelial matrix (2). VWF also enhances secondary hemostasis by functioning as a carrier protein for factor VIII, increasing its half-life fivefold (3). Released into the circulation as enormous multimers reaching >12 MDa in size and >15 μm in length (4, 5), VWF provides a multivalent platform for platelet aggregation at sites of tissue of injury.

VWF is exclusively synthesized by endothelial cells and megakaryocytes and, as the largest soluble protein in vertebrates, undergoes extensive processing to generate its extreme length and to facilitate its storage and secretion. Early in biosynthesis, pro-VWF monomers dimerize in the endoplasmic reticulum through inter-monomer disulfide bonds in the C-teminal cystine-knot (CK) domain (Fig 1.1B) (6). VWF then traffics to the Golgi, where the lower pH induces further non-covalent zipping up of proVWF dimers. At the C-terminus, the A2, A3 and D4 domains zip up into elongated, dimeric bouquets (Fig 1.1C) (7) that guide assembly of the N-terminal D domains into helical tubules (Fig 1.1D) (8). At the same time, proVWF dimers concatamerize through disulphide linkage at the N-terminus and the propeptide sequence is removed by furin cleavage (Fig 1.1E) (9).

Large VWF concatamers are targeted to cytoplasmic secretory granules, known as Weibel-Palade bodies (WPB), within endothelial cells (10). Thrombogenic stimuli, such as epinephrine, thrombin,

fibrin, histamine, and vasopressin, stimulate endothelial cells to release ultralarge VWF, which is secreted through a pore formed between WPB and the plasma membrane (11). Long VWF fibrils have been observed to extend from stimulated endothelial monolayers in the direction of flow (12), and it has been proposed that these fibrils represent self-assembly of multiple VWF concatamers unfurling in parallel from separate tubules (13). In addition to the ultralarge VWF stored within WPB, endothelial cells and megakaryocytes constitutively secrete smaller VWF fragments. Studies in chimeric pigs found that normal pigs engrafted with VWF deficient marrow were capable of normal thrombus formation. However, thrombus formation was never observed in VWF deficient pigs engrafted with normal bone marrow, suggesting that ultralarge VWF secreted by endothelial cells is the critical mediator of hemostasis (14).

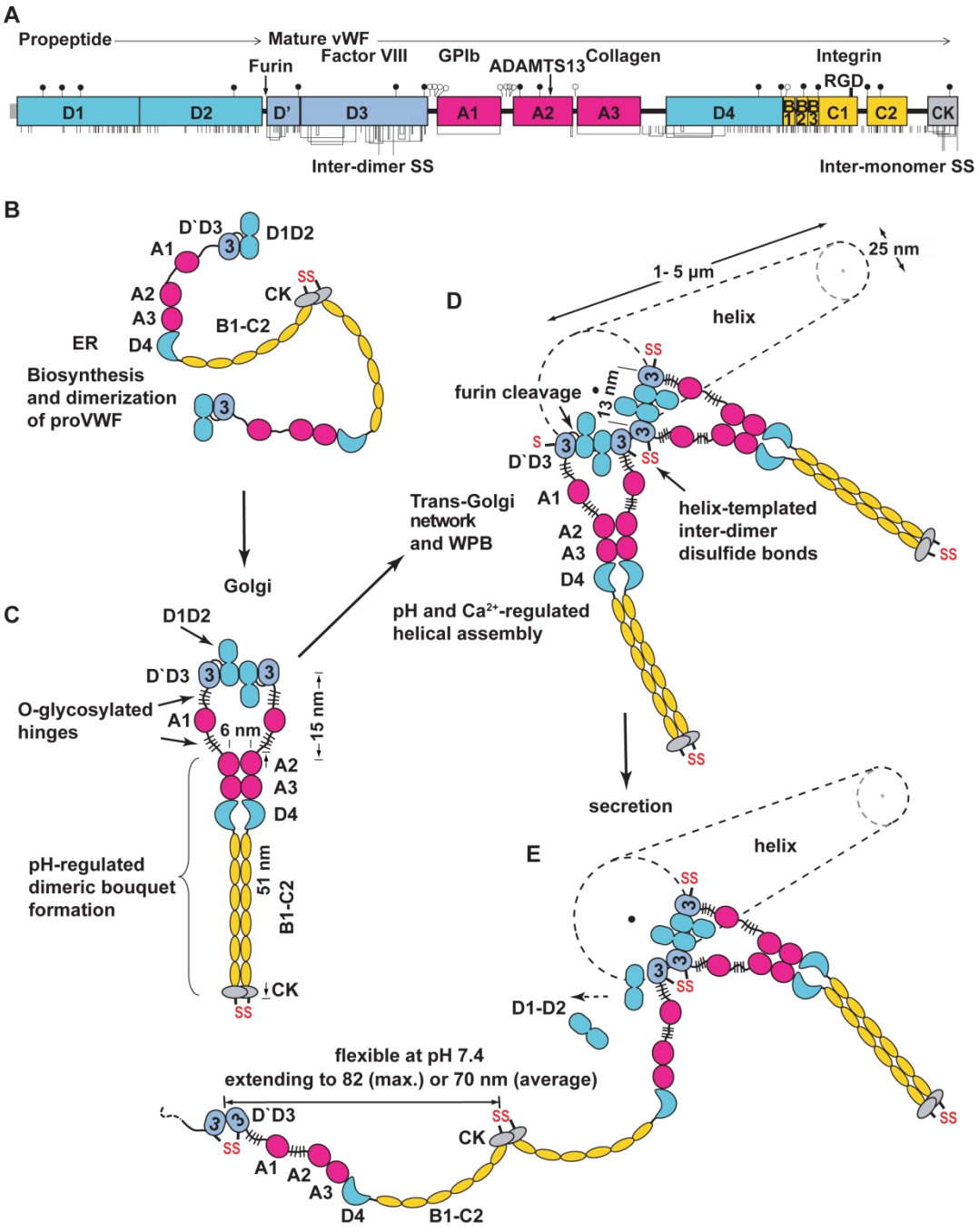

Fig 1.1 Structure of VWF concatamers. (A) Domain organization of VWF. Cysteines and disulfide bonds indicated beneath; N- and O-linked sites represented above as filled and open lollipops, respectively(15). (B) Biosynthesis and helical assembly of VWF concatamers. Homotypic interactions in the C-terminus guides helical assembly of proVWF dimers at the N-terminus.

VWF functional activity correlates with size

VWF thrombogenic activity correlates with size, with the largest VWF concatamers exhibiting the greatest thrombogenic potential (16). Ultralarge VWF is secreted from endothelial cells as long fibrils, which is then specifically cleaved by the metalloproteinase ADAMTS13 (a disintegrin and metalloprotease with a thrombospondin type 1 motif, member 13), producing a distribution of VWF concatamer lengths within the circulation. Absence of ADAMTS13 function results in the accumulation of ultralarge VWF concatamers, which inappropriately induce platelet aggregation in the life threatening condition known as thrombotic thrombocytopenic purpura (TTP) (17). In TTP, extensive microvascular thromboses result in tissue ischemia and infarction in multiple organs, defining a classic pentad of clinical features that include thrombocytopenia, microangiopathic hemolytic anemia, fever, neurologic symptoms and signs, and renal function abnormalities (18). TTP is treated with plasma exchange, which presumably reestablishes normal VWF size regulation by removing ADAMTS13 inhibitors and replenishing functional enzyme (19).

ADAMTS13 is a constitutively active enzyme whose activity is modulated by conformational changes within its VWF substrate. In particular, ADAMTS13 cleavage requires unfolding of the A2 domain. This unique mechanoregulatory mechanism is illuminated by the structure of VWF A2 (Fig 1.2B). The ADAMTS13 scissile bond is buried in a central β4 strand within A2 that is inaccessible in the native state (20). Under static conditions, VWF cleavage by ADAMTS13 only occurs in the presence of denaturing agents such as urea (21). Physiologically, VWF A2 unfolding is achieved through application of tensile force to the N and C termini (22) to allow enzyme access to the scissile bond.

VWF size regulation is critical to normal hemostasis and clinically useful for diagnosing thrombotic and bleeding disorders. The VWF multimer assay assesses VWF size distributions by separating VWF multimers in agarose gels (23). Whereas VWF concatamers are shifted to larger size distributions in TTP,

the absence of large VWF concatamers confirms a diagnosis of von Willebrand's disease (VWD), a bleeding diathesis resulting from reduced VWF function.

von Willebrand's Disease mutations illuminate VWF structural specializations

VWD encompasses a heterogeneous set of bleeding disorders that arise from various mutations within the VWF gene. Type 1 and 3 VWD describe quantitative deficiencies whereas type 2 VWD results from qualitative defects in protein function (24). VWD type 2 subtypes are defined by increased binding to platelets (type 2B), decreased binding to platelets (type 2M), reduced binding and stabilization of factor VIII (type 2N), and lack of high molecular weight VWF multimers (type 2A). Comprising 10% of all diagnoses, VWD 2A is the second most common VWD subtype and is characterized by the selective loss of high molecular weight multimers. Patients present with increased bleeding due to decreased VWF thrombogenicity. Type 2A may be further subdivided based on whether abnormal VWF size distributions arise from impaired VWF biosynthesis (Group 1) or increased cleavage by ADAMTS13 despite normal VWF multimer assembly and secretion (Group 2) (25). Both groups of VWD 2A mutations cluster within the A2 domain bearing the scissile bond for cleavage by ADAMTS13.

The gain of function phenotypes described in VWD 2B (increased platelet binding) and VWD 2A (increased VWD 2A proteolysis) provide fascinating insight into domain structure. VWD 2B mutations map to buried sites within VWF A1 (Fig 1.2A) (26) (27) and likely cause increased GPIb binding by inducing conformational changes within A1 that destabilize an alternative conformation with weaker binding ability. Such a two state model has yet to be described by crystallography. However, single molecule experiments suggest that distinct flexed and extended A1 conformations reflect the unique ability of the domain to withstand high shear forces in arteriolar flow (28). Similarly, VWD 2A mutations map to the interior of the A2 domain, and are hypothesized to increase A2 susceptibility to cleavage by altering the force sensitivity to A2 unfolding.

Paradoxically, gain of function mutations in VWD 2B present with increased bleeding. Instead of the thrombosis one might expect with increased VWF-GPIb binding (29), VWD 2B patients exhibit smaller VWF multimers which may be due to increased clearance of large multimers as well as markedly elevated VWF proteolysis (29). Platelet bound VWF is hypothesized to experience greater hydrodynamic forces that are transmitted to the A2 cleavage domain to allow unfolding. The increased susceptibility of VWD 2B to proteolysis highlights the remarkable force sensing ability of the A2 cleavage domain.

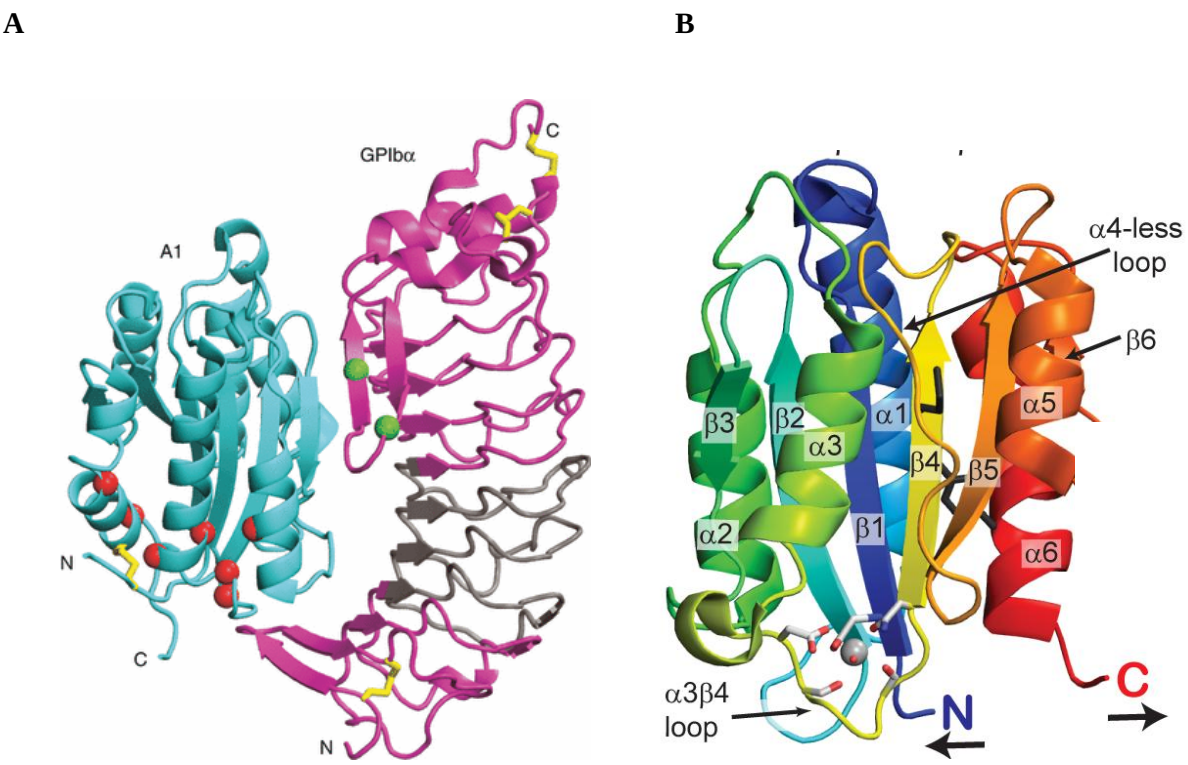

Fig 1.2. A1 and A2 domain structures. (A) Crystal structure of GPIb and VWF A1 complex. Disulphides shown with gold sticks. VWD 2B mutations in A1, marked with red spheres, are buried within A1 and do not contact GPIb. Figure from (13). (B) Structural specializations of VWF A2. The scissile bond at Y1605/M1606 (grey sidechains) is buried within a central β4 strand. Elongational force, experienced by VWF concatamers and applied to the N and C termini, as shown by arrows, renders A2 susceptible to ADAMTS13 cleavage. A calcium binding site lies within the α3-β4 loop.

Shear stress regulates VWF cleavage

Given its large size, VWF is particularly susceptible to hydrodynamic force and fluid shear stress critically regulates VWF size distributions (12). In addition to the genetic mutations described in von Willebarnd's disease, decreased VWF function has also been attributed to pathologic changes in shear environments experienced by VWF. Acquired VWD is a clinically described bleeding disorder thought to arise from increased shear forces inducing increased shear-stress-induced proteolysis of VWF. The clinical association between severe aortic stenosis and gastrointestinal bleeding, known as Heyde's syndrome, is linked to changes in VWF multimer distribution.

A study of patients being evaluated for aortic valve replacement demonstrated that patients with aortic stenosis exhibited bleeding disorders associated with pathologically small VWF multimers. Bleeding and VWF size distribution completely normalized upon surgical repair of pathologic shear with aortic valve replacement (30). Acquired VWD has also been described in patients implanted with mechanical circulatory support devices (31), which pathologically increase shear forces experienced in the circulation. These characterizations of bleeding disorders arising from mechanical defects underscore the role of mechanical force in regulating VWF function.

Shear stress activates VWF adhesivity

Large VWF concatamers are critical for platelet aggregation in arteriolar flow. Though platelets may form stable adhesive interactions with collagen (32) and fibrinogen (33), these direct platelet interactions do not form under the high shear forces experienced in arterioles. Stable platelet adhesion at shear rates above 500 s^{-1} requires VWF (32), which is specialized to function in high shear environments.

VWF thrombogenicity increases with increasing shear (32) and circulating VWF does not normally bind platelets under low shear. Shear stress induces conformational changes in VWF structure that were first described using atomic force microscopy (34). Above a critical shear rate, exposure of VWF to shear flow induces VWF to transition from collapsed to extended conformations.

Dynamic visualization of fluorescently labeled VWF within a microfluidic flow chamber demonstrated that VWF globule-stretch transitions are reversible, occur on very short time scales, and correlate with adhesive function (5). Theory from polymer physics predicts the transition at a well-defined threshold flow rate, $\varepsilon_{critical}$, at which the polymer immediately unravels from a globular to stretched conformation (35). Consistent with this model, VWF adopted a stretched conformation reaching 15 μm above a critical shear rate of 5,000 s^{-1}. Once the hydrodynamic shear was reduced below this critical shear rate, VWF immediately relaxed back to its compact, globular state. These conformational dynamics were correlated with adhesive function by monitoring binding to a collagen coated substrate. Below the critical shear rate, VWF adhered to the collagen coated surface in a coiled state, whereas above the critical shear rate, VWF formed spider like networks, suggesting that shear-induced unfolding of globular VWF activates adhesion to the vessel wall (35). This critical transition is dictated by hydrodynamic forces, which vary throughout the vasculature but are enhanced during hemostasis and in pathologic thrombotic states.

Hydrodynamic forces within the vasculature

VWF experiences a range of hydrodynamic forces that regulate its function. Fluid forces are governed by geometry, fluid viscosity, and fluid speed. In most vessels, flow is laminar (36) and defined by parallel fluid layers gliding past each other with a parabolic velocity profile. Fluid velocity is highest in the centerline and decreases to zero along the vessel walls (Fig 1.3A). The velocity difference between adjacent fluid layers is defined by the shear rate (s^{-1}), and is zero at the centerline and maximal at the vessel wall. Shear stress (dyn/cm^2) is the force per unit area exerted by viscous lamina traveling at different velocities, and is directly related to shear rate by fluid viscosity. Accordingly, shear stress is zero along the central axis of flow and maximal along the vessel wall.

Physiologic shear rates are lowest in large veins (< 20 s^{-1} (37)) and highest in narrow arterioles (5000 s^{-1} (38)). Extremely high shear stresses are encountered in the setting of severe stenosis and may exceed

40,000 s^{-1} (39). A crude approximation of force experienced by a platelet tethered to the vessel wall may be estimated by the wall shear stress experienced by a 2.8 μm sphere. Given the typical range of fluid velocities and vascular dimensions *in vivo* (40), force estimates range from 0.5-5 pN in veins, 7-20 pN in large arteries, 10-40 pN in arterioles, and 20-1000 pN in stenotic vessels.

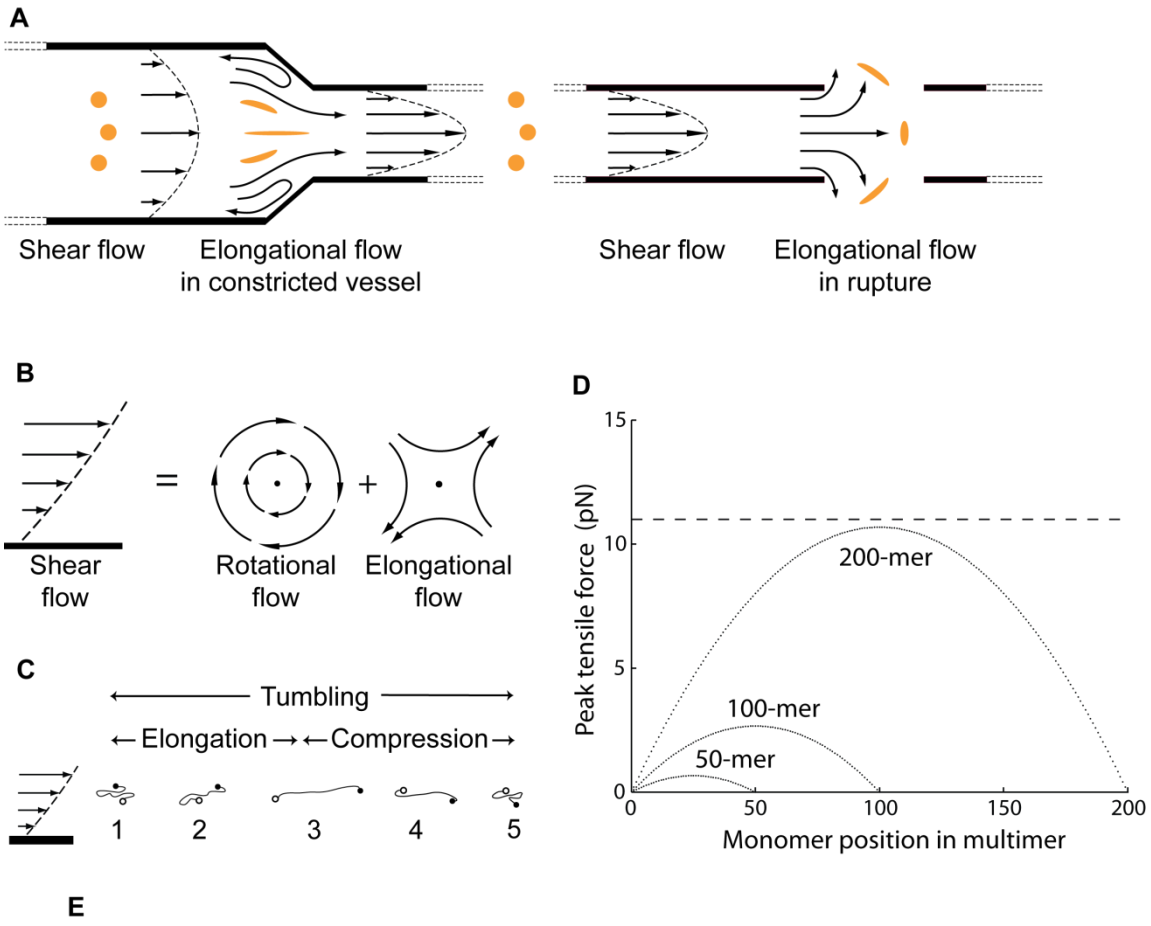

Fig 1.3. Hydrodynamic forces experienced by VWF. (A) Shear flow, transitioning to elongational flow with changes in vessel geometry. Round, orange spheres emphasize the effect of elongational flow in deforming globular polymer into an elongated chain. (B) Shear flow tends to rotate and elongate polymers. (C) Schematic of VWF elongating, compressing, and tumbling in shear flow. (D) Peak tensile force experienced by VWF A2 monomer scales with the square of concatamer length.

VWF is regulated by elongational flow

Hydrodynamic forces experienced by flexible VWF concatamers may be understood through polymer physics. Shear flow can be conceptualized as the superposition of rotational and elongational components (Fig 1.3B). Rotational flow tends to rotate but not deform particles, causing VWF globules to tumble. In contrast, elongational flow induces large deformations in polymer shape, inducing VWF to stretch from a collapsed conformation into an elongated chain (41). Such elongational flows are responsible for the previously described globule to stretch transition required for activating VWF adhesivity.

Elongational forces develop in regions of shear gradients, which are created by changes in vessel geometry and have been implicated in driving thrombus formation. Fluid escaping from ruptured vessels travels orthogonal to the direction of blood flow and undergoes purely elongational flow (Fig 1.3A). Elongational flows are also enhanced by changes in vessel shape, which may arise from atherosclerotic lesions or bifurcations. Interestingly, atherosclerotic lesions are known to preferentially develop at sites of carotid bifurcation (42), where elongation forces dominate. Indeed, recent studies have demonstrated that shear gradients drive thrombus formation (43). Applying a blunted needle to stenose the lumen of mesenteric arterioles in mice, Nesbitt et. al used high-resolution intravital microscopy to observe resulting thrombus formation induced by shear microgradients. Platelets preferentially adhered in low-shear zones, and aggregate size was determined by the magnitude of shear microgradients. The authors attributed their findings to mechanosensory platelet activation. However, these low shear zones are also significant for rapid shear deceleration which greatly enhances elongation forces, and it would be interesting to understand the role VWF plays in mediating shear-gradient induced thrombus formation.

Elongation forces also develop during the natural process of hemostasis. Healthy endothelium produces compounds, such as nitric oxide and prostacyclin, to inhibit platelet aggregation and enhance vasodilation. Upon vessel injury, blood vessels immediately constrict to limit blood flow and minimize the surface area of the open lesion. This initial vasospasm is mediated by sympathetic nerve reflexes,

which stimulate smooth muscle contraction. Vasoconstriction is also mediated by agonists released by endothelial cells and platelets. As activated platelets aggregate to plug the injured site, several compounds are released from their storage granules, including serotonin, epinephrine, platelet activating factor, and thromboxane A_2 (44). These agonists reverse the natural vasodilated state by profoundly reinforcing vasoconstriction of the affected vessels by promoting intracellular calcium influx within vascular smooth muscle cells. Vasoconstriction itself may also reinforce hemostasis by enhancing elongational forces to activate VWF thrombogenicity.

In addition to functioning as the first step of hemostasis, vasospasm is implicated in thrombotic pathologies. Vasospasm of the coronary arteries, which perfuse heart tissue, causes a variant of chest pain known as variant or Prinzmetal's angina. Such vasospasms lead to myocardial infarction and are thought to be caused by autonomic stimulation (45) and/or endothelial dysfunction (46). Vasospasm has also been implicated in initiating thrombotic occlusions in the absence of coronary atherosclerosis. A study of patients at risk for myocardial infarction found, on post-mortem exam, fresh, laminar thrombi that led to complete coronary occlusion at the sites of vasospasm (47). Vasoconstriction, whether due to atherosclerotic narrowing, functioning in hemostasis, or precipitating thrombotic pathologies, plays a clear role in hemostasis and thrombosis and may regulate VWF function by enhancing elongational flows.

Numerical simulations of VWF dynamics confirm the relevance of elongation forces to VWF regulation (48). Modeling VWF concatamers as a series of dimers interconnected by hydrophobic interactions, Sing et. al demonstrated that VWF unfolding is strongly regulated by elongational flows. They determined the critical flow rates at which VWF globules unfold to a fully extended chain, and demonstrated that elongational flows unfold VWF at flow rates that are two orders of magnitude below those corresponding to pure shear.

VWF adhesive function is determined by the structural transiton of globular to stretched conformations that respond most sensitively to elongational flows. Thus, the magnitude of shear

gradients (which give rise to elongation forces), rather than absolute shear rates, is most relevant for predicting hemostatic activation of VWF function.

Single molecule force spectroscopy

In addition to inducing global changes in structure, force regulates VWF function at the level of individual domains. Recent advances in single molecule techniques have yielded powerful insight into the mechanisms of VWF mechanoregulation. In particular, experiments using single molecule optical tweezers have elucidated the role of mechanical force in regulating VWF cleavage (22, 49, 50) and A1 platelet binding (28), and are pioneering new concepts in how mechanical force regulates biological processes.

Understanding how mechanical force effects changes in protein conformation requires control over force application and assessment of conformational change. Bulk experimental methods lack both the precision and sensitivity to monitor conformational dynamics. Conventional techniques for applying force to bulk solutions, including vortex and stir, result in a heterogeneous distribution of forces experienced by each molecule. Furthermore, detection of conformational change is limited by the averaging of many molecules in different states. Single molecule techniques overcome these barriers by removing the confounding effects of ensemble averaging and offering precise control over individual molecules.

Conventional methods of single molecule force application include Optical Tweezers, Magnetic Tweezers, and Atomic Force Microscopy (51). Optical Tweezers offers high spatial (0.1-2 nm) and temporal resolution within a 0.1-100 pN force range that is relevant to hydrodynamic forces experienced in the vasculature, as well as typical forces required for protein unfolding (52). Optical Tweezers rely on the balance of optical "scattering" and "gradient" forces which stabilize particles slightly beyond the waist of a focused laser beam. Near the center of the trap, optical forces behave as a linear "Hookean" spring (53), exerting a force proportional to the object's displacement from the center of the trap (Fig

1.4A). Because optical trapping relies on the energy absorbed from highly focused laser beams, photodamage is avoided by manipulating biological molecules with functional handles. DNA handles, which function as physical spacers, are a popular strategy for linking functionalized proteins because they minimize nonspecific interactions and provide a molecular signature for force calibration via the well-studied force extension curve of DNA (54). Several methods for linking DNA to protein have been reported, including disulfide exchange (55) and click chemistry to alkyne modified groups (56). With careful calibration, optical trapping functions as a highly sensitive tool for quantitative measurements and has proven a powerful tool for probing biological interactions.

A1-GPIb interactions are specialized to withstand hydrodynamic forces

VWF is remarkable for its ability to maintain platelet adhesion under high shear, an interaction mediated by VWF A1 binding of platelet GPIb. To test the hypothesis that A1-GPIb is specialized to resist mechanical force, single molecule optical tweezers were employed to characterize the response of A1-GPIb binding to tensile force. The bimolecular interaction between VWF A1 and platelet GPIb was isolated using a novel method for measuring binding and unbinding of a receptor and ligand in a single molecule (ReaLiSM) (Fig 1.4A). Crystal structures of the A1-GPIb complex demonstrate that the globular A1 domain interacts with leucine-rich repeats within the concave face of GPIb (Fig 1.2A) (57, 58). Informed by their close proximity and lack of contribution to the complex interface, 43 and 26 residue polypeptide linkers were attached to the C-terminus of VWF A1 and N-terminus of GPIb to form ReaLiSM constructs to investigate using optical tweezers.

The mechanical response of A1-GPIb was studied by suspending the ReaLiSM construct between functionalized DNA handles attached to polystyrene beads controlled by the laser trap (Fig 1.4A). During repeated cycles of increasing and decreasing force, abrupt increases and decreases in the length of the tether reflected unbinding and rebinding events, respectively, (Fig 1.4B) that were verified by fitting the extension and contraction lengths to the wormlike chain model of entropic elasticity. Dissociation between A1 and GPIb was monitored over different pulling rates. Whereas low pulling rates rates yielded

narrow, unimodal distributions of bond rupture events, higher pulling rates clearly resolved a bimodal distribution of rupture forces. Taken together, the data collapse onto two exponential decreases in bond lifetime with increasing force, with different kinetics dominating at forces below and above a threshold force of around 10 pN (Fig 1.4C). The kinetic model implicates two distinct pathways for dissociation of the GPIb-A1 bond, a two state "flex-bond" (Fig 1.4D) that broadens the distribution of forces that A1-GPIb can withstand. This model supports the specialized function of VWF A1 over a wide range of shear environments. Interestingly, above 10 pN, the GPIb-A1 exhibits a second state that is more force resistant. Thus, the high shear environment of arteriolar flow reinforces GPIb-A1 binding, underscoring the structural specializations of VWF for functioning under high force.

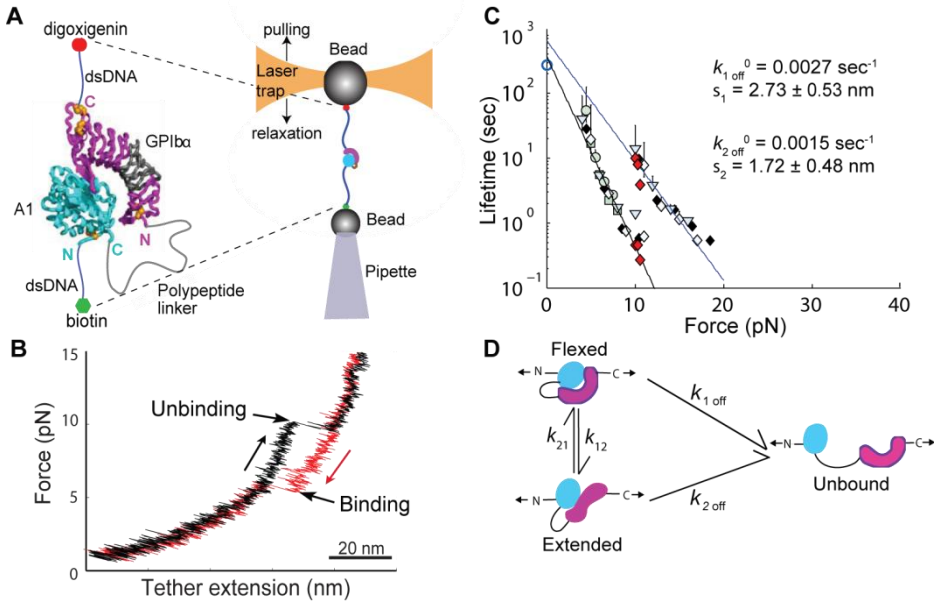

Fig 1.4. A1-GPIb bond is specialized to withstand high force. (A) Schematic of ReaLiSM fusion construct containing the A1 domain, a polypeptide linker, and GPIb. (B) Representative cycle of unbinding and rebinding, measured as abrupt changes in tether extension during pulling (black) and relaxation (red). (C) Kinetic measurements from rupture force histograms collapse onto a two state model. (D) Schematic model of flex bond.

A2 unfolding regulates VWF cleavage

VWF A2 exhibits several structural features that allow it to be regulated by hydrodynamic forces in the circulation (Fig 1.2B). The ADAMTS13 scissile bond is buried in a central β4-strand within A2 that is inaccessible in its native state. Compared to neighboring domains, VWF A2 lacks a long-range disulfide bond to protect the domain against unfolding by elongational (tensile) force exerted on VWF concatamers. Additional structural features appear to render the domain more sensitive to force. In place of an α4 helix, an "α4-less" loop is thought to slow refolding to promote cleavage site accessibility (20). Unlike the neighboring A1 and A3 domains, VWFA2 contains two N-linked glycosylation sites (Asn 1574 and Asn 1515) which may help confer rigidity, as removal of Asn1574 results in increased proteolysis (59). A2 also features a unique calcium binding site (silver) demonstrated to protect VWF against ADAMTS13 cleavage (60) and enhance refolding (50). These unique features within VWF A2 promote dynamic accessibility of the buried scissile bond.

Single molecule studies have demonstrated that ADAMTS13 cleavage requires unfolding of the A2 domain to expose the scissile bond (22). To mimic the transmission of tensile force within intact VWF through the A1 and A3 domains, DNA handles were covalently linked to the N and C termini of A2 (Fig 1.5A). The single molecule construct was suspended between polystyrene beads, one suctioned onto the tip of a micropipette and another trapped within the focus of an infrared laser beam. In response to repeated cycles of force increase, force decrease, and force clamping, the A2 domain exhibited robust unfolding and refolding behavior that manifested as abrupt tether extensions (Fig 1.5B). These force extension discontinuities were confirmed as full unfolding of the A2 domain by fitting to the worm-like chain model of entropic elasticity. Even under different optical setups, the length increases at different forces agreed well with the expected length of an unfolded polymer chain of 177 residues (22, 50).

At a given force application (loading) rate, A2 unfolded across a distribution of forces. Histograms of A2 unfolding forces across increasing loading rates were well modeled by biophysical

theory that predicts the most likely unfolding force to exhibit a logarithmic dependence on loading rate (61). Refolding was investigated by clamping the tether at a low force between each cycle of force increase and decrease to allow the A2 domain an opportunity to refold.

Refolding was found to be sensitive to time, force, and calcium conditions. The probability of refolding significantly increased with decreased force and increased time. Calcium chelation significantly decreased the probability of refolding (49, 50). Calcium binding has been demonstrated to protect the domain from cleavage by ADAMTS13 (60) and calcium mediated stabilization against thermal denaturation has also been described (49, 50). Loss of calcium stabilization in enhancing A2 refolding may contribute to the mechanism of R1597 VWD 2A mutations, which reside in the calcium binding loop and form a critical salt bridge interaction with Asp1498, the only reside that binds calcium outside of the α3β4 loop (Fig 1.2B). VWD 2A mutations destabilize the domain and may increase susceptibility to cleavage by altering the force sensitivity to unfolding and refolding (A. Xu and T.A. Springer, unpublished).

The requirement of A2 unfolding for ADAMTS13 cleavage was demonstrated by mechanically unfolding A2 in the absence or presence of ADAMTS13, and then clamping at 5 pN to wait for ADAMTS13 cleavage to manifest as a drop of the force on the tether to 0 pN (Fig 1.5D). No cleavage of folded A2 was observed, and fits of the cleavage rates at three different enzyme concentrations to the single-molecule Michaelis-Menten equation yielded cleavage kinetics comparable to bulk phase experiments on ADAMTS13 cleavage of peptide substrates (62, 63). Studies on the A1-A2-A3 tridomain are consistent with studies on isolated A2, demonstrating that force-induced A2 unfolding is required for cleavage in the presence of neighboring domains as well (64, 65).

Under the rate of force loading on VWF concatamers in plasma, unfolding of single wild-type A2 molecules is predicted to be most likely at 11 pN. Hydrodynamic forces roughly scale with dimension, as larger molecules cross more shear lamina when extended. Tensile force on the center of an extended

VWF concatamer in shear scales with N^2, where N is the number of monomers. Estimation of the force on VWF concatamers *in vivo* in shear flow are consistent with the maximal length of VWF concatamers found in plasma (Fig 1.3D). The second power dependence of force exerted on the center of the concatamer predicts that cleavage occurs near the center, optimizing VWF for the most efficient proteolysis into smaller multimers (22).

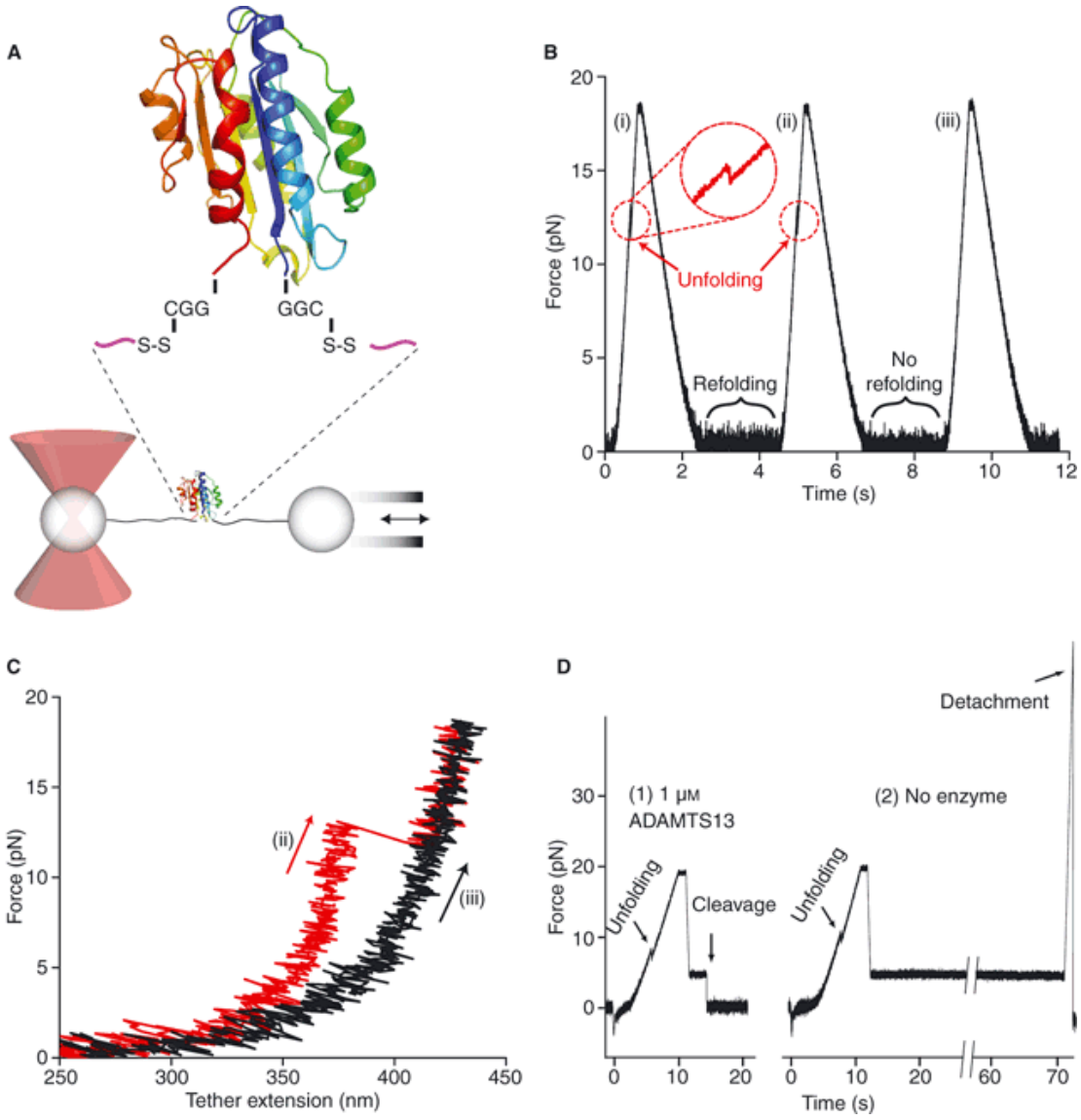

Fig 1.5. Single Molecule demonstration of A2 domain unfolding, refolding and mechanoenzymatic cleavage. (A) Schematic of single molecule A2 construct. Tensile force controlled by movement of micropipette and reported by displacement of bead from center of optical trap. (B) Repeated cycles of force increase and decrease reveal reversible A2 unfolding. (C) Force extension curves discriminate between folded (red) and unfolded (black) constructs. (D) Representative traces demonstrating requirement of A2 unfolding for ADAMTS13 cleavage.

Hydrodynamic forces dictate several layers of VWF function

VWF is a remarkable molecule that is structurally specialized to respond to its hydrodynamic environment. Mechanical force regulates several layers of VWF function. Elongational forces mediate the global transition from quiescent VWF in a collapsed state, to adhesive, elongated VWF chains. Tensile force experienced by the A2 cleavage domain offers protective feedback regulation against overactive thrombogenicity, exposing a scissile bond for ADAMTS13 cleavage that attenuates VWF thrombogenicity. The A1 domain features a unique "flex-bond" with two conformational states to increase its dynamic range of force resistance and enable stable interactions with platelets even under the high shear environment of arteriolar flow.

VWF's force sensitive functions are governed by elongational flows arising from shear gradients. Simulations have demonstrated that VWF is exquisitely sensitized to elongational flow, as VWF unfolds at flow rates two orders of magnitude lower for elongational flow compared to pure shear. During physiologic vasoconstriction in hemostasis, elongational flows are enhanced and may help reinforce the hemostatic process. Elongational flows may also be implicated in thrombotic pathologies, as they are induced by certain geometries known to be prothrombotic, such as carotid artery bifurcations. Furthermore, existing pathologies, such as stenosis due to atherosclerotic narrowing, may be reinforced by increased elongational flow. In future studies, it will be interesting to understand the role VWF plays in mediating shear-gradient induced thrombus formation to gain deeper insight into hemodynamic conditions that result in thrombotic pathologies.

References

1. Huang J, Roth R, Heuser JE, & Sadler JE (2009) Integrin α(v)β(3) on human endothelial cells binds von Willebrand factor strings under fluid shear stress. *Blood* 113(7):1589-1597.
2. Roth GJ, Titani K, Hoyer LW, & Hickey MJ (1986) Localization of binding sites within human von Willebrand factor for monomeric type III collagen. *Biochemistry* 25:8357-8361.
3. Brinkhous KM, *et al.* (1985) Purified human factor VIII procoagulant protein: comparative hemostatic response after infusions into hemophilic and von Willebrand disease dogs. *Proc Natl Acad Sci U S A* 82(24):8752-8756.
4. Hoyer LW & Shainoff JR (1980) Factor VIII-related protein circulates in normal human plasma as high molecular weight multimers. *Blood* 55(6):1056-1059.
5. Schneider SW, *et al.* (2007) Shear-induced unfolding triggers adhesion of von Willebrand factor fibers. *Proc. Natl. Acad. Sci. U S A* 104:7899-7903.
6. Wagner DD, Lawrence SO, Ohlsson-Wilhelm BM, Fay PJ, & Marder VJ (1987) Topology and order of formation of interchain disulfide bonds in von Willebrand factor. *Blood* 69(1):27-32.
7. Zhou Y, *et al.* (2011) A pH-regulated dimeric bouquet in the structure of von Willebrand factor. *EMBO J* 30(19):4098-4111.
8. Huang RH, *et al.* (2008) Assembly of Weibel-Palade body-like tubules from N-terminal domains of von Willebrand factor. *Proc Natl Acad Sci U S A* 105(2):482-487.
9. Lynch DC, Williams R, Zimmerman TS, Kirby EP, & Livingston DM (1983) Biosynthesis of the subunits of factor VIIIR by bovine aortic endothelial cells. *Proc Natl Acad Sci U S A* 80(9):2738-2742.
10. Wagner DD, Olmsted JB, & Marder VJ (1982) Immunolocalization of von Willebrand protein in Weibel-Palade bodies of human endothelial cells. *J Cell Biol* 95(1):355-360.
11. Berriman JA, *et al.* (2009) Structural organization of Weibel-Palade bodies revealed by cryo-EM of vitrified endothelial cells. *Proc Natl Acad Sci U S A* 106(41):17407-17412.
12. Dong JF, *et al.* (2002) ADAMTS-13 rapidly cleaves newly secreted ultralarge von Willebrand factor multimers on the endothelial surface under flowing conditions. *Blood* 100:4033-4039.
13. Springer TA (2011) Biology and Physics of von Willebrand Factor Concatamers. *J Thromb Haemost* 9(Supplement 1):130-143.
14. Nichols TC, *et al.* (1995) Function of von Willebrand factor after crossed bone marrow transplantation between normal and von Willebrand disease pigs: effect on arterial thrombosis in chimeras. *Proc Natl Acad Sci U S A* 92(7):2455-2459.
15. Springer TA (2011) Biology and physics of von Willebrand factor concatamers. *J Thromb Haemost* 9 Suppl 1:130-143.
16. Moake JL, Turner NA, Stathopoulos NA, Nolasco LH, & Hellums JD (1986) Involvement of large plasma von Willebrand factor (vWF) multimers and unusually large vWF forms derived from endothelial cells in shear stress-induced platelet aggregation. *J Clin Invest* 78(6):1456-1461.
17. Chow TW, *et al.* (1998) Increased von Willebrand factor binding to platelets in single episode and recurrent types of thrombotic thrombocytopenic purpura. *Am J Hematol* 57(4):293-302.
18. Ultmann EAaJ (1966) Thrombotic thrombocytopenic purpura: report of 16 cases and review of the literature. *Medicine* 45:139.
19. Rock GA, *et al.* (1991) Comparison of plasma exchange with plasma infusion in the treatment of thrombotic thrombocytopenic purpura. Canadian Apheresis Study Group. *N Engl J Med* 325(6):393-397.
20. Zhang Q, Zhou Y-F, Zhang C-z, & Springer TA (2009) Structural specializations of A2, a force-sensing domain in the ultralarge vascular protein von Willebrand factor. *Proc. Natl. Acad. Sci. U S A* 106(23):9226-9231.
21. Furlan M (1996) Von Willebrand factor: molecular size and functional activity. *Ann Hematol* 72(6):341-348.

22. Zhang X, Halvorsen K, Zhang CZ, Wong WP, & Springer TA (2009) Mechanoenzymatic cleavage of the ultralarge vascular protein, von Willebrand Factor. *Science* 324:1330-1334.
23. Krizek DR & Rick ME (2000) A rapid method to visualize von willebrand factor multimers by using agarose gel electrophoresis, immunolocalization and luminographic detection. *Thromb Res* 97(6):457-462.
24. Sadler JE (2005) New concepts in von Willebrand disease. *Annu Rev Med* 56:173-191.
25. Sadler JE, *et al.* (2006) Update on the pathophysiology and classification of von Willebrand disease: a report of the Subcommittee on von Willebrand Factor. *J Thromb Haemost* 4(10):2103-2114.
26. Hampshire D (2009) ISTH-SSC VWF Online Database.
27. Emsley J, Cruz M, Handin R, & Liddington R (1998) Crystal structure of the von Willebrand Factor A1 domain and implications for the binding of platelet glycoprotein Ib. *J. Biol. Chem.* 273:10396-10401.
28. Kim J, Zhang C, Zhang X, & Springer TA (2010) A mechanically stabilized receptor-ligand flex-bond important in the vasculature. *Nature* 466(7309):992-995.
29. Saba HI, Saba SR, Dent J, Ruggeri ZM, & Zimmerman TS (1985) Type IIB Tampa: a variant of von Willebrand disease with chronic thrombocytopenia, circulating platelet aggregates, and spontaneous platelet aggregation. *Blood* 66(2):282-286.
30. Vincentelli A, *et al.* (2003) Acquired von Willebrand syndrome in aortic stenosis. *N Engl J Med* 349(4):343-349.
31. Crow S, *et al.* (2010) Acquired von Willebrand syndrome in continuous-flow ventricular assist device recipients. *Ann Thorac Surg* 90(4):1263-1269; discussion 1269.
32. Savage B, Almus-Jacobs F, & Ruggeri ZM (1998) Specific synergy of multiple substrate-receptor interactions in platelet thrombus formation under flow. *Cell* 94(5):657-666.
33. Ikeda Y, *et al.* (1991) The role of von Willebrand factor and fibrinogen in platelet aggregation under varying shear stress. *J Clin Invest* 87(4):1234-1240.
34. Siedlecki CA, *et al.* (1996) Shear-dependent changes in the three-dimensional structure of human von Willebrand factor. *Blood* 88:2939-2950.
35. Sing CE & Alexander-Katz A (2010) Globule-Stretch Transitions of Collapsed Polymers in Elongational Flow Fields. *Macromolecules* 43(7):3532-3541.
36. Goldsmith HL & Turitto VT (1986) Rheological aspects of thrombosis and haemostasis: basic principles and applications. ICTH-Report--Subcommittee on Rheology of the International Committee on Thrombosis and Haemostasis. *Thromb Haemost* 55(3):415-435.
37. Kroll MH, Hellums JD, McIntire LV, Schafer AI, & Moake JL (1996) Platelets and shear stress. *Blood* 88(5):1525-1541.
38. Tangelder GJ, Slaaf DW, Arts T, & Reneman RS (1988) Wall shear rate in arterioles in vivo: least estimates from platelet velocity profiles. *Am J Physiol* 254(6 Pt 2):H1059-1064.
39. Strony J, Beaudoin A, Brands D, & Adelman B (1993) Analysis of shear stress and hemodynamic factors in a model of coronary artery stenosis and thrombosis. *Am J Physiol* 265(5 Pt 2):H1787-1796.
40. Alevriadou BR ML (1994) Rheology. *Thrombosis and Hemorrhage*, ed Loscalzo J SA (Blackwell Scientific Publications, Boston, MA), pp 369-381.
41. Smith DE, Babcock HP, & Chu S (1999) Single-polymer dynamics in steady shear flow. *Science* 283(5408):1724-1727.
42. Zarins CK, *et al.* (1983) Carotid bifurcation atherosclerosis. Quantitative correlation of plaque localization with flow velocity profiles and wall shear stress. *Circ Res* 53(4):502-514.
43. Nesbitt WS, *et al.* (2009) A shear gradient-dependent platelet aggregation mechanism drives thrombus formation. *Nat Med* 15(6):665-673.
44. Sherwood L (2011) Human Physiology: From Cells to Systems. *Human Physiology: From Cells to Systems*, ed Horne N (Jack Caarey, Pacific Grove, CA), pp 380-386.

45. Sakata K, Shirotani M, Yoshida H, & Kurata C (1997) Iodine-123 metaiodobenzylguanidine cardiac imaging to identify and localize vasospastic angina without significant coronary artery narrowing. *J Am Coll Cardiol* 30(2):370-376.
46. Kawano H, *et al.* (2001) Menstrual cyclic variation of myocardial ischemia in premenopausal women with variant angina. *Ann Intern Med* 135(11):977-981.
47. Maseri A, *et al.* (1978) Coronary vasospasm as a possible cause of myocardial infarction. A conclusion derived from the study of "preinfarction" angina. *N Engl J Med* 299(23):1271-1277.
48. Sing CE & Alexander-Katz A (2010) Elongational flow induces the unfolding of von Willebrand factor at physiological flow rates. *Biophys J* 98(9):L35-37.
49. Jakobi AJ, Mashaghi A, Tans SJ, & Huizinga EG (2011) Calcium modulates force sensing by the von Willebrand factor A2 domain. *Nat Commun* 2:385.
50. Xu AJ and Springer TA. Calcium stabilizes the von Willebrand factor A2 domain by promoting refolding. *Proc Natl Acad Sci U S A* 109(10):3742-3747.
51. Neuman KC & Nagy A (2008) Single-molecule force spectroscopy: optical tweezers, magnetic tweezers and atomic force microscopy. *Nat Methods* 5(6):491-505.
52. Bustamante C, Chemla YR, Forde NR, & Izhaky D (2004) Mechanical processes in biochemistry. *Annu Rev Biochem* 73:705-748.
53. Neuman KC & Block SM (2004) Optical trapping. *Rev Sci Instrum* 75(9):2787-2809.
54. Bustamante C, Smith SB, Liphardt J, & Smith D (2000) Single-molecule studies of DNA mechanics. *Curr Opin Struct Biol* 10(3):279-285.
55. Cecconi C, Shank EA, Dahlquist FW, Marqusee S, & Bustamante C (2008) Protein-DNA chimeras for single molecule mechanical folding studies with the optical tweezers. *Eur Biophys J* 37(6):729-738.
56. Agard NJ, Baskin JM, Prescher JA, Lo A, & Bertozzi CR (2006) A comparative study of bioorthogonal reactions with azides. *ACS Chem Biol* 1(10):644-648.
57. Huizinga EG, *et al.* (2002) Structures of glycoprotein Iba and its complex with von Willebrand factor A1 domain. *Science* 297:1176-1179.
58. Dumas JJ, *et al.* (2004) Crystal structure of the wild-type von Willebrand factor A1-glycoprotein Ibalpha complex reveals conformation differences with a complex bearing von Willebrand disease mutations. *J. Biol. Chem.* 279:23327-23334.
59. McKinnon TA, Chion AC, Millington AJ, Lane DA, & Laffan MA (2008) N-linked glycosylation of VWF modulates its interaction with ADAMTS13. *Blood* 111(6):3042-3049.
60. Zhou M, *et al.* (2011) A novel calcium-binding site of von Willebrand factor A2 domain regulates its cleavage by ADAMTS13. *Blood* 117(17):4623-4631.
61. Evans E & Ritchie K (1997) Dynamic strength of molecular adhesion bonds. *Biophys. J.* 72:1541-1555.
62. Gao W, Anderson PJ, Majerus EM, Tuley EA, & Sadler JE (2006) Exosite interactions contribute to tension-induced cleavage of von Willebrand factor by the antithrombotic ADAMTS13 metalloprotease. *Proc Natl Acad Sci U S A* 103(50):19099-19104.
63. Zanardelli S, *et al.* (2006) ADAMTS13 substrate recognition of von Willebrand factor A2 domain. *J Biol Chem* 281(3):1555-1563.
64. Wu T, Lin J, Cruz MA, Dong JF, & Zhu C (2010) Force-induced cleavage of single VWF A1A2A3-tridomains by ADAMTS-13. *Blood* 115(2):370-378.
65. Ying J, Ling Y, Westfield LA, Sadler JE, & Shao JY (2010) Unfolding the A2 domain of von Willebrand factor with the optical trap. *Biophys J* 98(8):1685-1693.

Chapter II:

Single Molecule Optical Tweezers

Amy J. Xu

Introduction and Theory

First reported by Arthur Ashkin and Steven Chu in 1986 (1), optical trapping has since enjoyed a range of applications leading to many important insights in biology and physics. The principles governing optical tweezers may be understood through a simple balance of optical forces. Dielectric particles near the waist of a focused laser beam experience (1) a "scattering force" from the transfer of momentum from impinging photons, pushing the particle axially away from the laser focus, as well as (2) a "gradient force" pointing in the direction of the intensity gradient when the refractive index of the particle exceeds that of the medium. When a highly focused laser beam creates a steep enough intensity gradient, the pull of the "gradient force" towards the laser focus counters the push of the "scattering force", stabilizing the dielectric particle at an equilibrium position slightly beyond the waist of the laser beam.

Theoretical calculations of these optical forces are well established in the limits of spherical Mie (diameter >> wavelength) and Raleigh (diameter << wavelength) particles. Mie particles may be treated with a ray optics approach. When the refractive index of the particle exceeds the refractive index of the medium, the particle acts as a weak positive lens, with refraction exerting a net backwards pull on the particle towards the beam focus (Fig 2.1) to counter the scattering force acting in the opposite direction.

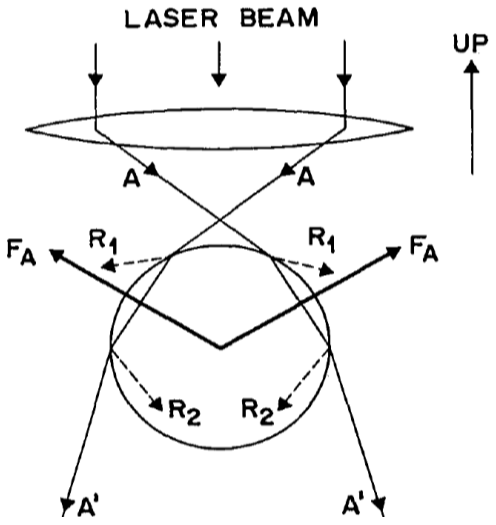

Figure 2.1. ***Ray Optics description of "gradient force" for Mie particle.***

A typical pair of rays A from a highly focused laser beam principally refract through a particle of higher refractive index to emerge as rays A', resulting in forces F_A directed towards the laser focus (1)**.**

Raleigh particles experience a scattering force from the re-radiation of absorbed light, pointing in the direction of incident light. The "gradient" force results from induced dipoles interacting with the inhomogeneous electric field, and for particles with refractive indices greater than the medium, points towards the laser focus. These forces may be directly calculated (Equations 1-3) and their ratio strongly depends on wavelength (λ^5), particle size (r^{-3}) and focal spot size (ω_o^{-2}). There is a weaker dependence on refractive indices, with optimal trapping occurring for high refractive indices (n_b^2) but with $n_{particle}$ only slightly higher than n_{medium} (small $m=n_{particle}/n_{medium}>1$ to maintain direction). Thus, the gradient force most effectively overcomes scattering when particles are small, refractive indices are large, lasers are highly focused, and wavelengths are long.

Equations 1-3: ***Optical Forces for Raleigh Particles.***

Stable trapping requires F_{grad}: F_{scat} to be greater than 1. (1)

$$F_{\text{scat}} = \frac{I_0}{c}\frac{128\pi^5 r^6}{3\lambda^4}\left(\frac{m^2-1}{m^2+2}\right)^2 n_b. \qquad (1)$$

$$F_{\text{grad}} = -\frac{n_b}{2}\alpha\nabla E^2 = -\frac{n_b^3 r^3}{2}\left(\frac{m^2-1}{m^2-2}\right)\nabla E^2. \qquad (2)$$

$$R = \frac{F_{\text{grad}}}{F_{\text{scat}}} = \frac{3\sqrt{3}}{64\pi^5}\frac{n_b^2}{\left(\frac{m^2-1}{m^2+2}\right)}\frac{\lambda^5}{r^3 w_0^2} \geq 1, \qquad (3)$$

Laser power does not factor into the balance of optical forces, but is critical for overcoming Brownian motion. The potential of the gradient force, $U=n_b\alpha E^2/2$, is directly proportional to the particle's polarizability α (defined in Equation 2), which strongly depends on laser power (E^2) and particle size (r^3). Similar to the balance of optical forces, there is a weaker dependence on refractive indices. Thus, the gradient force most effectively overcomes thermal fluctuations with powerful lasers and large particles.

Accounting for these two requirements for stable trapping, it may be shown that gradient forces most effectively overcome scattering and Brownian motion for (i) highly focused (small ω_o), powerful (high E), long wavelength (high λ) lasers, (ii) operating in a high refractive index medium, (iii) acting on a particle with a refractive index slightly greater than that of the medium (small m >1). Particle size is bound by the opposing effects of particle radius on the gradient/scattering ratio (r^{-3} dependence) vs. gradient force potential (r^3 dependence). The

particle must be small enough for gradient forces to dominate scattering, yet large enough for the gradient force potential to overcome Brownian motion.

Practically, these constraints allow stable optical trapping for 25nm-10μm particles (1). Although refractive indices affect trapping stability, most biologic applications dictate water as the relevant media. The strong dependence of trapping stability on wavelength is limited by increasing absorption by water towards the infrared. Thus, increased power for stable trapping must be balanced by the potential for photodamage. For most applications, stable trapping is best achieved with 25nm-10μm particles (with refractive indices slightly greater than water) using moderately powerful near-IR lasers sharply focused through objectives with high numerical aperture.

Ashkin and Chu's first report of a single-beam gradient force optical trap in 1986 described the stable trapping of particles in water using a 514.5 nm laser, ranging from a 10 μm glass sphere (100 mW) to 26 nm silica particles (1.4 W) (1). In addition to maximum laser power, small particle trapping was also limited by extensive photodamage, assessed by drastic changes in scattering intensity, to latex, polystyrene, and viral particles (2). Shifting to a 1.06 μm IR laser resulted in much improved optical traps with less optical damage, allowing the "damage-free" (as assessed by reproductive viability and maintenance of cellular integrity) trapping of bacteria, yeast, red blood cells, and organelles (3).

With these advances in damage-free trapping, optical tweezers have been used for manipulation of the microscopic world. Optical tweezers have been used to isolate new high temperature enzymes from a heterogeneous population (4) and are even being investigated for clinical applications of *in vitro* fertilization (5). Alternatively, precise control of photodamage in

so called “laser scissors” has been applied as a tool for intracellular surgery to modify the chromosomes of living cells (6). The advent of new technologies, such as holographic (7) and zone plate optical tweezers (8), allow for multiplexed optical trapping with exciting high throughput applications, such as particle sorting.

Quantitative Optical Trapping

Despite these advances in optical traps, optical forces remain generally insufficient to stably trap biological macromolecules themselves. An alternative method of handling biological specimens biochemically couples the molecule of interest to microscopic dielectric particles, which (i) enables stable trapping, (ii) protects the specimen from photodamage and (iii) functions as a probe for quantitative measurements. Near the center of the trap, optical forces behave as a linear “Hookean” spring (9), exerting a force proportional to the object’s displacement, Δx , from the center of the trap. With careful calibration, optical trapping functions as a highly sensitive tool for quantitative measurements.

Force calibration of quantitative optical trapping relies on the careful determination of trap stiffness. Given a bead of known radius free in solution (far from any surface), trap stiffness may be determined by exploiting Stokes relation for viscous drag. Trap stiffness may also be determined by measuring positional variance and applying the equipartition theorem ($^1/_2\ k_BT = {}^1/_2\ k_{trap}\langle x^2\rangle$), or by directly measuring the momentum transfer from scattered light (9). Excursions of the bead from the center of the trap report the force exerted or experienced by the molecule of interest. Because optical trapping optimally measures piconewton forces, the range most relevant for protein dynamics, optical tweezers as force spectroscopy has proven a powerful tool for probing biological interactions.

Single Molecule Applications

Optical Tweezers enable the application and measurement of force on single particles, thus allowing for direct observation of molecular events no longer obscured by bulk ensemble averaging. By elucidating the individual fluctuations hidden within bulk measurements, important insights have been gained into a wide range of biophysical mechanisms, including motor proteins, nucleic acid enzymes, and protein unfolding.

An early target for single molecule study using optical tweezers was the motor protein kinesin, a mechanoenzyme that couples ATP hydrolysis for linear movement along microtubules. Kinesins are dimer molecules known to produce active movement against a load. Cellular functions include cargo transport and cytoskeletal force generation during mitosis. Initial studies on kinesin directly coupled silica beads to kinesin motor molecules, followed by careful placement onto microtubules immobilized on a coverslip (Fig 2.2A). Careful titration of kinesin molecule concentrations during silica bead coupling favored observations of single kinesin molecules. The force produced by kinesin molecules was estimated by applying an opposing optical trap force to try to stop bead movement (10). Improving upon these initial studies, Svoboda and Block introduced an optical trapping interferometer allowing for feedback stabilization of a three-axis piezoelectric stage. In this way, they effectively damped the Brownian motion of the sphere to achieve the resolution of detailing the discrete 8nm steps of a single kinesin molecule (11). Thermal noise may also be reduced with a dual trap system (Fig 2.2B). Taking advantage of the dramatic increase in resolution upon discarding noise caused by symmetric motion (12), such a dual-trap system allowed the direct observation of individual 0.34 nm base-pair steps of transcribing RNA polymerase translocating on a DNA dumbbell suspended between trapped polystyrene beads (13).

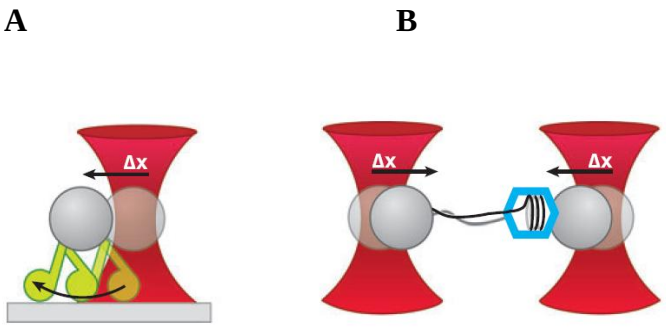

Figure 2.2. ***Optical Tweezer Studies of Kinesin Motors and Bacteriophage***

(A) Molecular motor activity monitored by directly attaching the motor to the bead (14). Motions of biological systems may also be revealed via length changes between two coupled beads. (B) Bacteriophage protein activity assessed through changes in DNA length assessed by the relative motion of beads from two optical traps(14). The dual trap geometry exploits symmetric motion to limit the effect of thermal noise on force spectroscopy measurements (12).

Optical force spectroscopy has also been applied to characterize folding-unfolding transitions in single molecules of titin, a filamentous protein fundamental for maintaining passive tension within sarcomeres of muscle (15). The precision of sensitivity of optical tweezers have made it an attractive platform for studying the mechanosensitivity of VWF, and is the basis for the single molecule experiments presented in this thesis.

Until recently, biological systems have mainly been characterized through chemical interactions. Optical tweezers offer a compelling system for understanding the effects of force on molecular interactions. Driven by technological advances in the field, commercial optical trapping systems are becoming increasingly sophisticated and versatile. As they become more

and more accessible to biologists, they are sure to change the way in which we understand biomolecular interactions and the role of force in biological systems.

References

1. Ashkin A, Dziedzic JM, Bjorkholm JE, & Chu S (1986) Observation of a single-beam gradient force optical trap for dielectric particles. *Opt Lett* 11(5):288.
2. Ashkin A & Dziedzic JM (1987) Optical trapping and manipulation of viruses and bacteria. *Science* 235(4795):1517-1520.
3. Ashkin A, Dziedzic JM, & Yamane T (1987) Optical trapping and manipulation of single cells using infrared laser beams. *Nature* 330(6150):769-771.
4. Huber R, *et al.* (1995) Isolation of a hyperthermophilic archaeum predicted by in situ RNA analysis. *Nature* 376(6535):57-58.
5. Wright G, Tucker MJ, Morton PC, Sweitzer-Yoder CL, & Smith SE (1998) Micromanipulation in assisted reproduction: a review of current technology. *Curr Opin Obstet Gynecol* 10(3):221-226.
6. Berns MW (1998) Laser scissors and tweezers. *Sci Am* 278(4):62-67.
7. Curtis JE, Koss BA, & Grier DG (2002) Dynamic holographic optical tweezers. *Opt. Commun.* 207(1-6):169-175.
8. Schonbrun E, Rinzler C, & Crozier KB (2008) Microfabricated water immersion zone plate optical tweezer. *Appl. Phys. Lett.* 92(7):3.
9. Neuman KC & Block SM (2004) Optical trapping. *Rev Sci Instrum* 75(9):2787-2809.
10. Block SM, Goldstein LS, & Schnapp BJ (1990) Bead movement by single kinesin molecules studied with optical tweezers. *Nature* 348(6299):348-352.
11. Svoboda K, Schmidt CF, Schnapp BJ, & Block SM (1993) Direct observation of kinesin stepping by optical trapping interferometry. *Nature* 365(6448):721-727.
12. Moffitt JR, Chemla YR, Izhaky D, & Bustamante C (2006) Differential detection of dual traps improves the spatial resolution of optical tweezers. *Proc Natl Acad Sci U S A* 103(24):9006-9011.
13. Abbondanzieri EA, Greenleaf WJ, Shaevitz JW, Landick R, & Block SM (2005) Direct observation of base-pair stepping by RNA polymerase. *Nature* 438(7067):460-465.
14. Moffitt JR, Chemla YR, Smith SB, & Bustamante C (2008) Recent advances in optical tweezers. *Annu Rev Biochem* 77:205-228.
15. Kellermayer MS, Smith SB, Granzier HL, & Bustamante C (1997) Folding-unfolding transitions in single titin molecules characterized with laser tweezers. *Science* 276(5315):1112-1116.

Chapter III:

Calcium Stabilizes the von Willebrand Factor A2 Domain by Promoting Refolding

Amy J. Xu and Timothy A. Springer

Abstract

von Willebrand Factor (VWF) is a large, multimeric plasma glycoprotein that critically mediates hemostasis at sites of vascular injury. Very large VWF multimers have the greatest thrombogenic activity, which is attenuated by cleavage in the A2 domain by ADAMTS13. ADAMTS13 proteolysis requires mechanical force to expose the scissile bond and is regulated by a calcium binding site within A2. In this study, we characterized the interaction between VWF A2 and calcium by examining the effect of calcium on VWF A2 stability and mechanical unfolding and refolding. Isothermal calorimetry yielded a calcium binding $K_d = 3.8 \pm 1.0$ μM and reversible thermal denaturation showed that 5 mM calcium stabilized the unfolding transition from 56.7 ± 0.1 to 69.1 ± 0.1 ^{o}C. Using optical tweezers to apply tensile force to single domains, we found that calcium did not affect VWF A2 unfolding, but rather enhanced refolding kinetics 5-fold, resulting in a 0.9 kcal/mol stabilization in the folding activation energy in the presence of calcium. Taken together, our data demonstrate that VWF binds calcium at physiologic calcium concentrations, and that calcium stabilizes VWF A2 by accelerating refolding.

Introduction

von Willebrand Factor (VWF) is a large plasma glycoprotein that critically mediates hemostasis at sites of vascular injury. Secreted by endothelial cells and platelets in response to thrombogenic stimuli, VWF circulates as ultralong, disulfide-bonded concatamers (1) reaching >12 MDa and >15 μm in size (2, 3). Each VWF monomer is comprised of multiple domains, including domains that bind clotting factor VIII, collagen, platelets, and integrins (1). The A2 domain contains a cleavage site recognized by the enzyme ADAMTS13 (a disintegrin and metalloprotease with a thrombospondin type 1 motif, member 13), which regulates VWF length. The largest VWF concatamers mediate the formation of a platelet plug through multivalent binding to collagen and platelet membrane glycoprotein Ib. Mutations within VWF cause von Willebrand's disease (VWD), a heterogeneous set of bleeding disorders that underscore VWF function in normal physiology (4).

VWF function is critically determined by concatamer length. Healthy individuals exhibit a heterogeneous distribution of VWF concatamers, whose size is regulated through specific cleavage by ADAMTS13. Absence of ADAMTS13 function causes thrombocytic thrombocytopenic purpura (TTP), a life threatening condition characterized by extensive microvascular thromboses that result in tissue ischemia and infarction. Neurologic symptoms and renal failure are often described, and the condition resolves upon replenishment of ADAMTS13 with plasma exchange (5). In contrast, genetic mutations that shift the VWF size distribution to smaller multimers, comprising Type 2 VWD, present with increased bleeding due to reduced VWF thrombogenicity (6). Subtype 2A VWD mutations cluster within the A2 domain, which bears the ADAMTS13 cleavage site, and whose structure illuminates mechanisms that regulate VWF cleavage (7).

Fluid shear stress is critical for VWF size regulation (8) and VWF A2 is remarkable for several structural features that render the domain sensitive to hydrodynamic forces exerted on VWF concatamers in the circulation. The ADAMTS13 scissile bond is buried in a central β4-strand within A2 that is inaccessible in the native state (Fig. 3.1A). Compared to neighboring domains, VWF A2 lacks a long-

range disulfide bond to protect the domain against unfolding by elongational (tensile) force exerted on VWF concatamers. Single molecule studies have demonstrated that ADAMTS13 cleavage requires unfolding of the A2 domain (7, 9) to expose the scissile bond. Furthermore, in place of an α4-helix, VWF A2 contains an "α4-less" loop which is thought to slow refolding to promote cleavage site accessibility (7). Thus, structural specializations within VWF A2 predict that reversible unfolding and refolding regulate VWF cleavage via dynamic accessibility of a buried scissile bond.

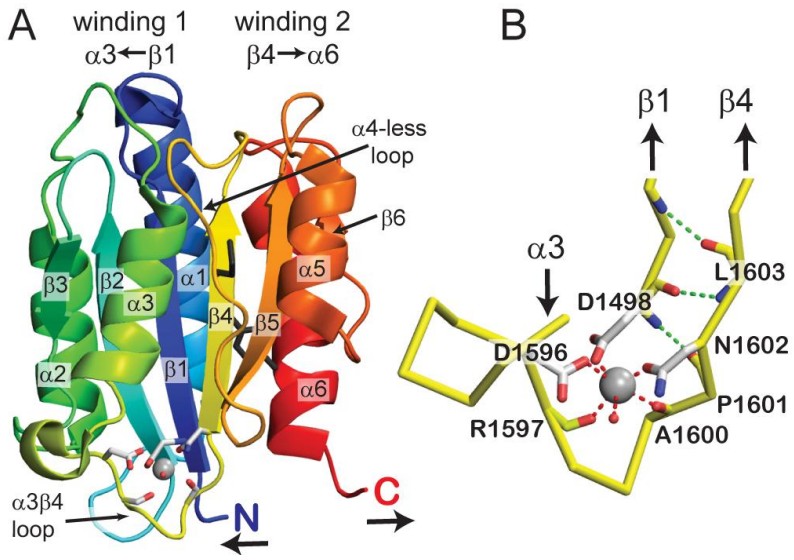

Figure 3.1. VWF A2 structure. A) A2 structural specializations. The scissile bond at Y1605/M1606 (grey sidechains) is buried within a central β4-strand. Elongational force experienced by VWF concatamers applied to the N and C termini renders A2 susceptible to ADAMTS13 cleavage. A calcium binding site in the α3-β4 loop lies at the junction between windings 1 and 2, topologically defined by their sequential arrangements of secondary structures in opposite directions. B) A2 calcium coordination. VWF A2 coordinates (red dashes) calcium (silver sphere) in octahedral geometry by six ligands, including a water molecule (small red sphere). Stabilizing hydrogen bonds are shown in green. The structure shown is a chimera containing residues 1495-1578 and 1602-1672 of 3GXB (9) and residues 1579-1601 of 3PPV (10). Figure made with PYMOL.

Recent studies have described a novel calcium binding site that is unique amongst VWF A domains, and likely another structural specialization that regulates VWF A2 force sensing. VWF coordinates calcium by four residues from the α3-β4 loop and a single residue from the N-terminal β1-strand (Fig. 3.1B) (10, 11). Calcium binding was not seen in an earlier structure due to a lattice contact that enforced a conformation of the α3-β4 that precluded calcium binding (7, 10). Unfolding of A2 is predicted to proceed from the C-terminus because, whereas the N-terminal β1-strand is clamped by hydrogen bonds in the center of the β-sheet, the C-terminal α6-helix is exposed and only locally hydrogen bonded (Fig. 3.1A). Furthermore, unfolding from the C-terminus of secondary structure elements in the sequence of α6, β6, α5, β5, α4-less loop and β4 exposes the minimal portion of the A2 domain required for maximal ADAMTS13 cleavage, as shown in peptide substrates (12). VWF A domains feature a "doubly wound" topology that juxtaposes two regions of sequentially arranged secondary structures. The α3-β4 loop lies at the junction between these two windings (Fig. 3.1A) and is thus in a strategic position to regulate A2 folding. In the sequential process of unfolding, the β4-strand bearing the scissile bond immediately precedes the α3-β4 loop. Cleavage assays of isolated A2 demonstrate that calcium binding protects the domain from cleavage by ADAMTS13 (10, 11), and protection against unfolding has also been reported (11). However, the quantitative details of how calcium stabilizes A2 remain to be defined.

In this study, we characterized the mechanisms underlying calcium stabilization of VWF A2. We derived thermodynamic parameters to quantitatively describe the interaction of calcium with VWF A2 and establish physiologic relevance. In parallel, we applied single molecule optical tweezers to functionally characterize the effect of calcium on A2 conformational dynamics. Combining such bulk and single molecule approaches, we gain a quantitative understanding of the conformational dynamics that regulate VWF cleavage.

Results

VWF A2 Binds Calcium with High Affinity

We employed isothermal calorimetry to determine the binding affinity of VWF A2 for calcium. Calcium was injected into a sample cell containing VWF A2 maintained at 25^{o}C. The A2 had been dialyzed against 5 mM EDTA, which was removed by gel filtration immediately before the experiment. The enthalpy of calcium binding monitored by measuring reaction heats after each calcium injection (Fig. 3.2A) was $\Delta H = -2.3 \pm 0.1$ kcal/mol. Binding of 0.84 moles calcium per mole of A2 suggested a single calcium binding site within A2. Fitting the binding isotherms to a single binding site model (Fig. 3.2B) yielded $K_d = 3.8 \pm 1.0$ μM. The relationships $\Delta G = -RT\ln(1/K_d)$ and $\Delta S = (\Delta H - \Delta G)/T$ yield $\Delta G = -7.4 \pm 0.3$ kcal/mol and $\Delta S = 17 \pm 1$ cal/mol/K. Our results demonstrate that VWF A2 binds calcium with high affinity and that the free energy of the A2-calcium complex is substantially lower than that of its isolated components.

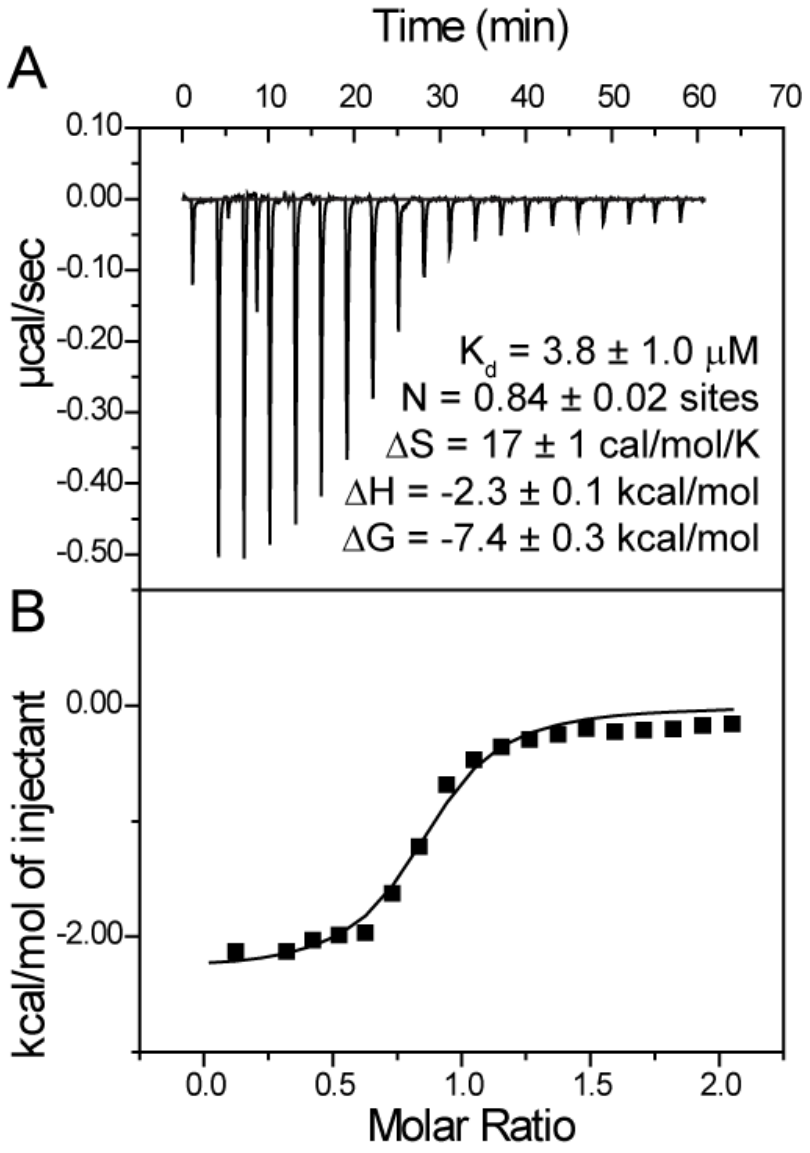

Figure 3.2. Calcium binding measurement by Isothermal Calorimetry. A) Calorimetry. Reaction heats measured from stepwise calorimetry performed at 25°C with 1.4 mM $CaCl_2$ injected against 140 µM A2 in the cell. B) Binding isotherm. Calcium binding affinity determined from calorimetry assuming single site binding.

Calcium Stabilizes A2 in Native Conformation

To assess the effect of calcium on VWF A2 thermodynamic stability, we obtained CD spectra to monitor changes in secondary structure. At 4°C, the CD spectra exhibited two negative bands at 222 and 208 nm (Fig. 3.3A, squares), a characteristic alpha helical spectrum (13) consistent with the high alpha helical content of VWF A2. Upon thermal denaturation, the spectra at 90°C lost alpha helical signature (Fig. 3.3A, triangles). Thermal denaturation changes were reversible. Cooling the protein back down to 4°C restored the alpha helical spectrum (Fig. 3.3A, circles). Similar changes in the native and denatured spectra were obtained in the presence and absence of calcium.

Calcium stabilized the native state of the A2 domain against thermal denaturation, monitored at 222 nm over a stepwise increase in temperature under equilibrium conditions of 3 minutes per °C (Fig. 3.3B). In the absence of calcium, VWF A2 remained stable until 50°C, with a midpoint melting temperature, T_m = 56.7 ± 0.1 °C. Chelating calcium with 1 mM EDTA did not change this transition, whereas 5 mM calcium stabilized the transition by 12°C (T_m = 69.1 ± 0.1 °C, Fig. 3.3B). No change was observed between 30 and 150 mM NaCl. Increasing calcium from 2mM to 5mM slightly increased thermal stability by 1.3 °C ± 0.1 °C, consistent with predictions for a two-state equilibrium (14).

To estimate changes in Gibbs free energy, thermal melts were analyzed according to Greenfield (15). Taking the 4°C and 90°C spectra to reflect the folded and unfolded states, respectively, the ratio of folded to unfolded A2 was determined from the signal at 222 nm. Experiments performed in the absence and presence of calcium were independently fit to the Gibbs Helmholtz equation of free energy (Fig. 3.3C; R^2 = 0.99). Extrapolating the fits to 25°C yielded Gibbs free energies of folding of -3.6 ± 0.8 kcal/mol in 5 mM calcium, and -2.3 ± 0.1 kcal/mol in the absence of calcium.

Figure 3.3. Calcium stabilization of VWF A2 against thermal unfolding measured by CD. (A) CD spectra of VWF A2 in native and denatured states reflect α-helical content. Representative wavelength scans at 4°C and 90°C reflect secondary structure of VWF A2 in native (squares) and denatured (triangles) states, respectively. Structural changes are similar in the presence (filled symbols) and absence of calcium (open symbols) and are reversible (gray circles). (B) Calcium stabilizes VWF A2 against thermal denaturation. CD signal at 222 nm monitored over a stepwise increase in temperature at equilibrium (3 minutes per °C). (C) Calcium decreases free energy of VWF A2 protein folding. Thermal melts were analyzed according to Greenfield (15). Equilibrium data shown over theoretical fits (R^2 = 0.99) with 95% confidence interval boundaries for free energy of protein folding.

Figure 3.3 (Continued)

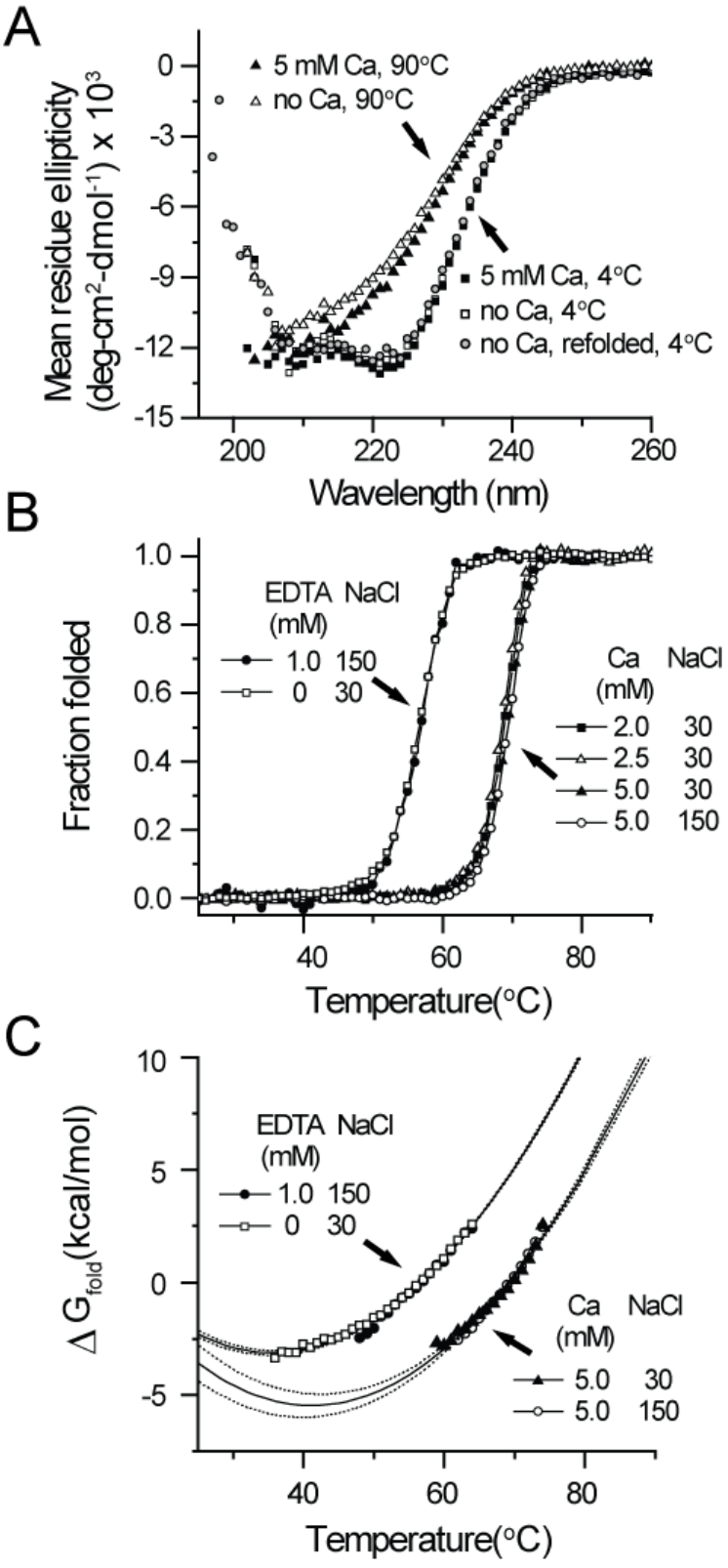

Calcium Does Not Affect VWF Unfolding

We used optical tweezers to examine the effect of calcium on the mechanoregulation of A2 by tensile force. VWF A2 was covalently linked to DNA handles and suspended between two polystyrene beads, one anchored to the tip of a micropipette and another trapped within the infrared dual beam laser focus of the optical tweezers (Fig. 3.4A). Changes in light momentum reflected excursions of the bead from the center of the trap, dx (Fig. 3.4A), and reported the force experienced by the protein-DNA tether with pN sensitivity. A2 unfolding was studied by monitoring force extension profiles of single tethers (Fig. 3.4B).

To quantitatively characterize VWF A2 mechanoregulation, 1881 pulls were analyzed under three experimental calcium conditions. A2 unfolding was reversible and robust (Fig. 3.4C) and the extension profiles of folded vs. unfolded constructs were well discriminated (Fig. 3.4B). In a representative trace, a folded construct was pulled at constant speed from 2 to 20 pN (Fig. 3.4B, black). At 14 pN, an abrupt discontinuity was observed with 37.4 nm extension (Fig. 3.4B, circle). Relaxation of the tether back down to the resting force (Fig. 3.4B, gray) retraced the force-extension profile of the unfolded construct. Once returned to a low force, tethers were held at constant position to allow refolding. At a moderate force of 3 pN, refolding was directly observed (Fig. 3.4D). However, at forces lower than 3 pN, the lower signal to noise ratio did not allow direct observations of refolding, and in most cases, refolding was measured indirectly from the presence or absence of unfolding in the subsequent pull (Fig. 3.4C).

Over a range of pulling rates, unfolding extensions displayed excellent agreement with full unfolding of VWF A2 when fit to the worm like chain (WLC) model of polymer elasticity (Fig.3.5A-D). Single molecule data obtained in the absence of calcium (Fig. 3.5A), under calcium chelating conditions (1 mM EDTA, Fig. 3.5B), and in the presence of 5 mM Ca (Fig. 3.5C) yielded contour lengths, or lengths of maximum extension, of 76.3 ± 1.3 nm, 75.0 ± 1.6 nm and 74.9 ± 1.3 nm, respectively. These results agreed with statistical significance within 4% (p<0.05) and demonstrate that calcium does not affect the

compliance of VWF A2 in the unfolded state. Fit to a global WLC model, the contour length was 75.6 ± 0.2 nm (Fig. 3.5D). In the crystal structure, the N-terminal and C-terminal residues Met1495 and Ser1671 are 1 nm apart (7). Thus, our data predict a 0.4 nm contour length per residue (75.6 + 1 = 76.6 nm divided by 177 residues), which agrees well with reported values (16), confirming the force extension discontinuities observed as full A2 unfolding under all calcium conditions.

Unfolding kinetics were determined by examining the forces at which A2 unfolding was observed. The force dependence of unfolding was extracted from rupture-force histograms obtained over a range of pulling speeds (20-160 nm/s), corresponding to force application rates of 0.1-10 pN/s, according to the Dudko-Hummer-Szabo method (17). Data were fit to a single-barrier kinetic model, $k = k_0 \exp(f\Delta x/k_bT)$, where the unfolding rate is determined by the unfolding rate at zero force, k_0, and an exponential dependence on force, f, multiplied by the distance to the transition state, Δx (18). Fit independently, the intrinsic unfolding rates at zero force, k_0, were 0.0034 s^{-1} (95% confidence interval 0.0032 to 0.0037 s^{-1}) and 0.0036 s^{-1} [0.0032 to 0.0042 s^{-1}] in the presence and absence of calcium, respectively, agreeing with statistical significance within 20% (p<0.05). A fit to all data in the presence and absence of calcium yielded k_0 = 0.0035 s^{-1} [0.0030 to 0.0041 s^{-1}] with a barrier to activation Δx = 2.5 ± 0.2 nm (R^2 = 0.97, Fig. 3.5E).

Figure 3.4. Monitoring protein unfolding using optical tweezers. (A) Experimental setup. Force spectroscopy performed on single A2 domains suspended between two polystyrene beads by DNA handles. Excursions of the bead from the center of the trap reported the force experienced by the single molecule construct. (B) Force extension profiles discriminate between unfolded and refolded constructs. Black trace follows ascent to 20 pN; gray curve follows relaxation to 2 pN. An abrupt force extension discontinuity during the ascent resolves the force extension profile of a folded vs. unfolded construct (circle). (C) A2 folding is reversible and robust. Representative pulling protocol: 40 nm/s pulling and relaxation rate (corresponding to force application rates of 0.5-2 pN/s) between 2 and 20 pN with 10 s pause at 2 pN. Force extension discontinuities are highlighted. No unfolding is seen in the third pull of this trace but protein refolds before the subsequent fourth pull. (D) Direct visualization of refolding. When the trap was held at a constant position, giving a force of 3 pN prior to refolding, refolding was observed directly (dashed box) as a change to ~4 pN in force during the refolding pause cycle.

Figure 3.4 (Continued)

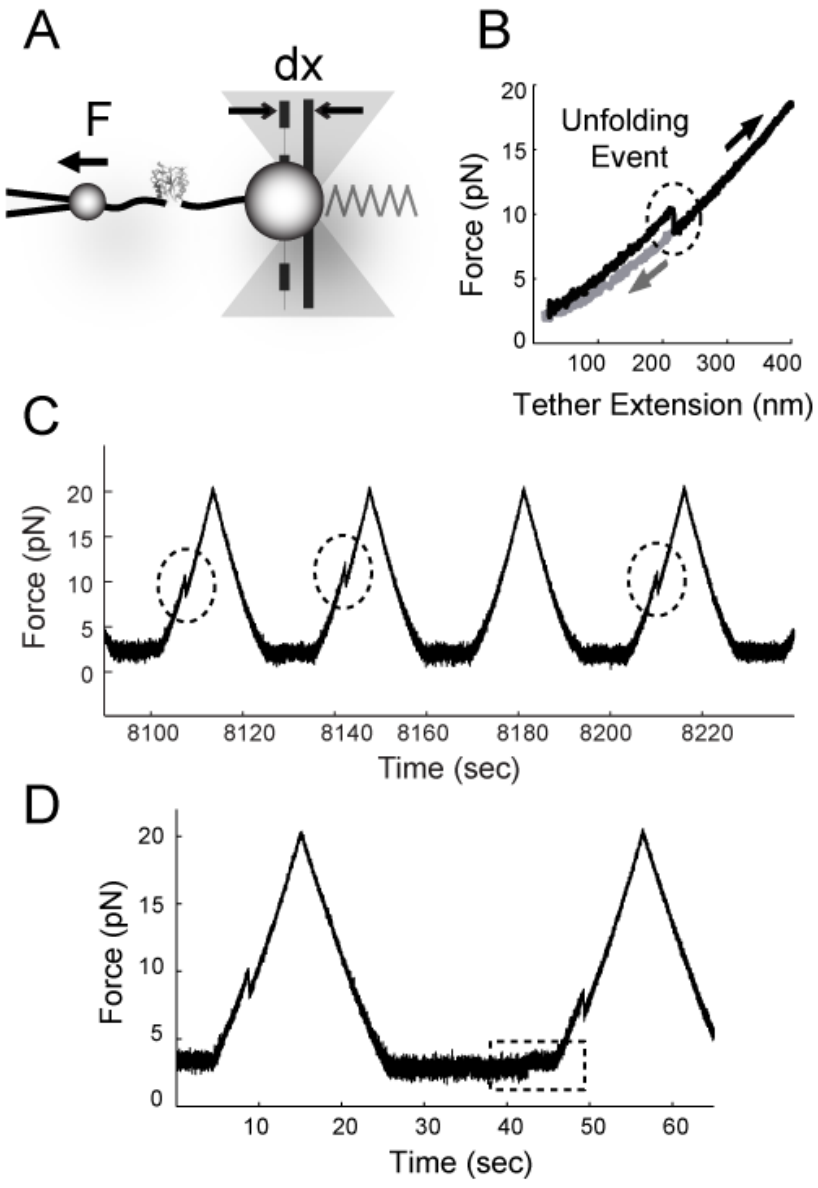

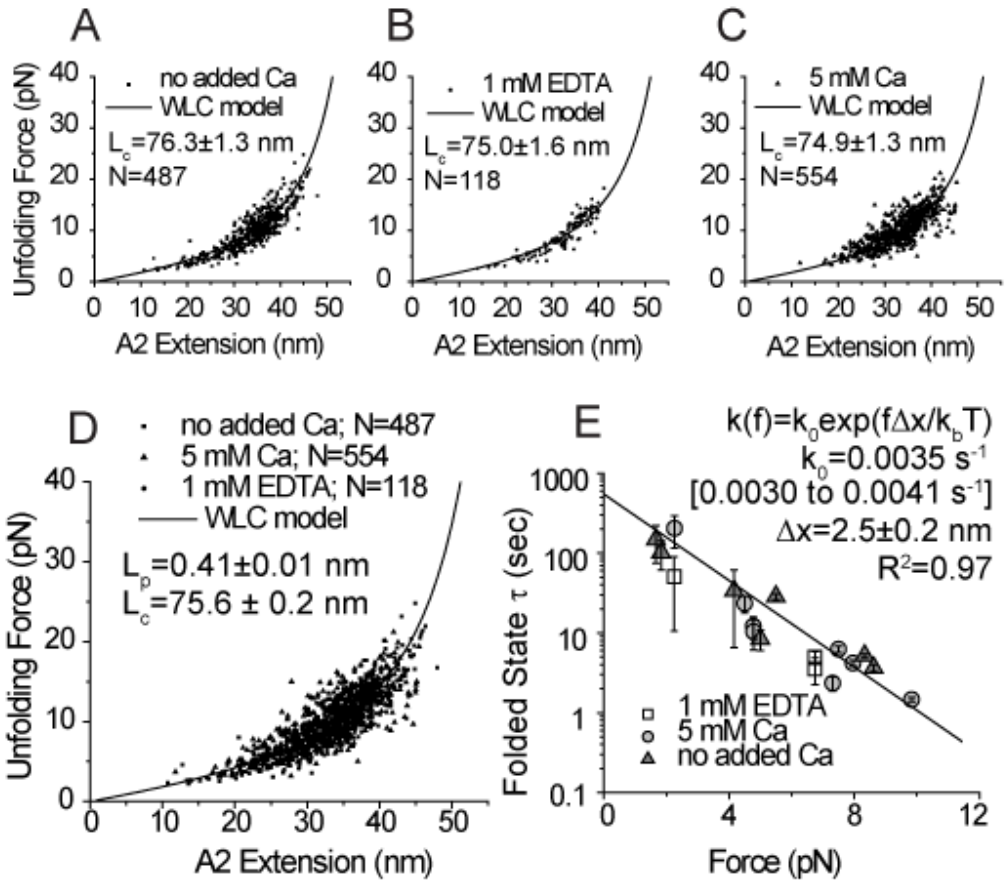

Figure 3.5. Lack of effect of calcium on A2 unfolding. (A-C) Lack of effect of calcium on the increase in extension upon A2 unfolding. Independent WLC fits for data collected in the absence of calcium (A), in the presence of calcium (B), and under calcium chelating conditions (C) demonstrate that calcium does not affect A2 compliance in the unfolded state, and that A2 exhibits full unfolding behavior under all three conditions. (D) Force extension discontinuities from all experiments fit to a single WLC model. Individual fits agreed within 4% ($p<0.05$). (E) Calcium does not affect kinetics of A2 unfolding. The force dependence of unfolding was derived from rupture-force histograms obtained over a range of pulling speeds according to the Hummer-Szabo-Dudko method (19). Errors shown are based on Poisson noise.

Calcium Enhances VWF Refolding

Refolding kinetics were assessed by monitoring the probability of refolding across consecutive pulling cycles on the same construct (Fig.3.4C). Single tethers were pulled then relaxed with loading rates of 0.1-10 pN/s. Once returned to a low force, the construct was held in constant position, corresponding to a constant force, to allow refolding (Fig. 3.4D). Protein refolding was monitored by force extension profiles (Fig. 3.4B) and the presence or absence of unfolding in a subsequent pull (Fig. 3.4C).

Observations of A2 refolding over many cycles (N = 786) demonstrated that A2 refolding was sensitive to force, time, and calcium. The probability of refolding significantly increased with decreased force (Fig 3.6A) and increased time (Fig. 3.6B). Calcium chelation significantly decreased the probability of refolding (Fig. 3.6C). Both in the presence and absence of calcium, the kinetics of refolding, k_f, were well fit by a single exponential dependence on the refolding rate at zero force, k_0, the square of force, f^2, and the compliance of the unfolded state, κ (18) (Fig. 3.6D-E). Under each calcium condition, data obtained at 1 pN, 2 pN and 3 pN were globally fit to a single set of parameters. The intrinsic kinetics of refolding at zero force, $k_{0,}$ in the presence and absence of calcium were $0.65 \pm 0.09\ s^{-1}$ and $0.14 \pm 0.03\ s^{-1}$, respectively. This 5-fold difference in refolding kinetics yields a 0.9 kcal/mol difference in the folding activation energy ($\Delta G^{U\text{-}TS}_{Ca} - \Delta G^{U\text{-}TS}_{no\ Ca} = 0.9$ kcal/mol) (Fig. 3.7A).

At moderate force, refolding was observed directly (Fig. 3.4D). In the presence of calcium at 3 pN, the lifetime of the unfolded state was 41 s (95% confidence interval 32 to 101 s, N = 40, 12 events observed directly), agreeing well with the unfolded state lifetime of 31 s expected from the kinetic model. In the absence of calcium, the 3 pN unfolded state lifetime was 96 s ([47 to 296 s], N = 23, 5 events observed directly), compared with 144 s predicted by the kinetic model. Thus, our direct observations of refolding agree well with the kinetic fits obtained from the much larger dataset of refolding probabilities.

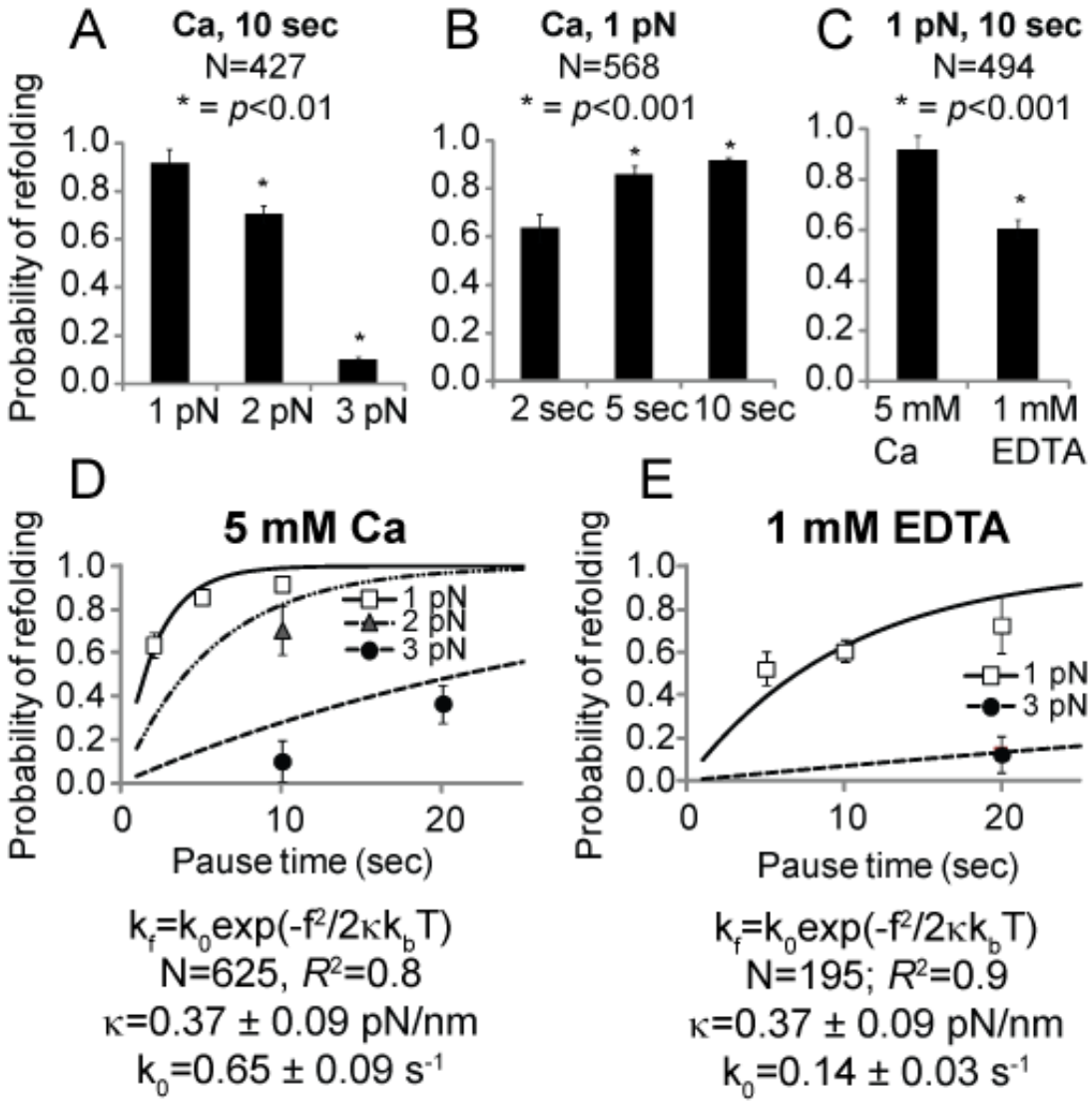

Figure 3.6. Calcium enhances kinetics of VWF A2 refolding. (A-C) Binary refolding statistics demonstrate that probability of refolding was sensitive to force (A), time (B), and calcium (C). (D-E) Force dependence of refolding kinetics. Refolding probabilities fit to a single exponential dependence of refolding kinetics on the square of applied force (18).

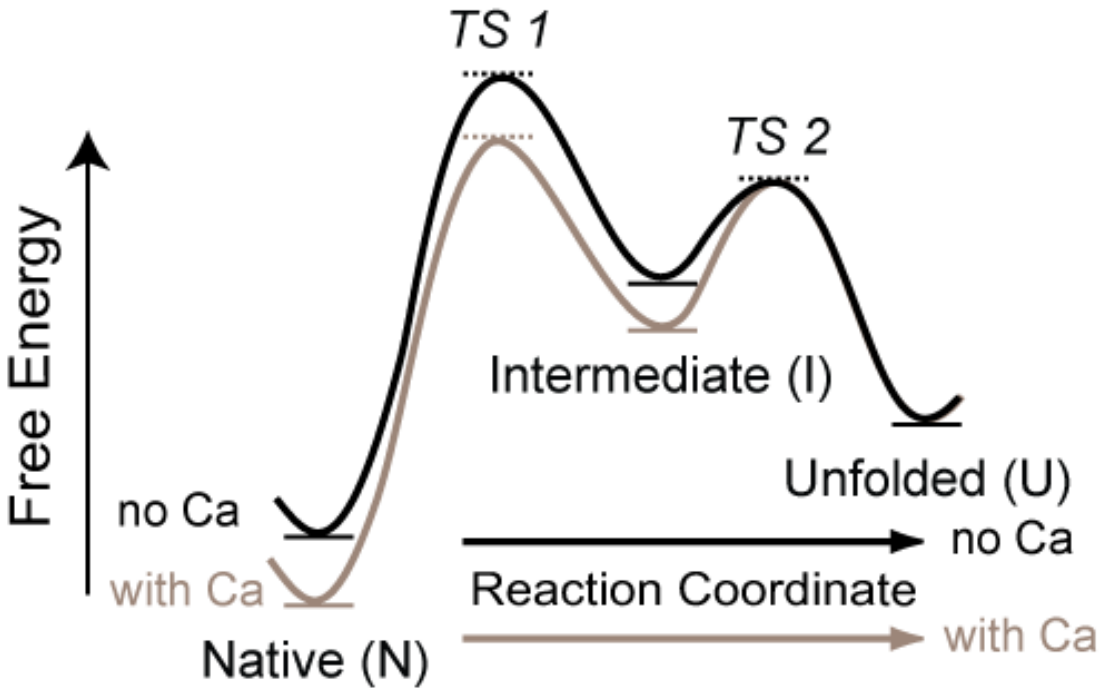

Figure 3.7. Proposed A2 energy landscape. Our proposed free energy landscape describing calcium stabilization of A2 features a calcium binding native state (N); a calcium-binding transition state (TS 1) that binds calcium with native-like coordination and is rate-limiting in both the unfolding and refolding directions; a high energy, calcium binding intermediate (I); a calcium free transition state (TS 2) in the refolding pathway; and a non-calcium binding unfolded state (U).

Discussion

In this study, we report quantitative bulk measurements of calcium binding and folding thermodynamics, and single molecule measurements of unfolding and refolding kinetics, to understand the mechanisms underlying calcium stabilization of VWF A2 against cleavage. Isothermal calorimetry yielded a 3.8 μM binding affinity between A2 and calcium. The ~1.1-1.3 mM free calcium in healthy human blood is greatly above this measured K_d. Thus, the calcium binding site is predicted to be saturated, establishing the relevance of calcium binding in VWF A2 under physiologic concentrations. Reversible thermal denaturation monitored using CD showed that calcium stabilized VWF A2 in the native state. We measured a thermodynamic stability shift of 12°C in 5 mM calcium, which is consistent with the apparent 19°C shift reported using fluorescent dye binding (11). Because our data were obtained under reversible conditions, we were able to estimate a folding free energy of -2.3 ± 0.1 kcal/mol in the absence of calcium, and -3.6 ± 0.8 kcal/mol in 5 mM calcium. The difference between these A2 unfolding energies predicts that 5 mM calcium stabilized the folded state by 1.3 ± 0.8 kcal/mol at 25°C. Single molecule measurements of A2 unfolding and refolding demonstrated that calcium stabilizes A2 by promoting refolding. Unfolding measurements revealed that calcium had little if any effect on unfolding behavior. In contrast, calcium accelerated refolding ~5-fold, lowering the activation barrier to refolding by 0.9 kcal/mol. Thus, we conclude that calcium stabilizes VWF A2 by promoting refolding.

Our thermodynamic and single molecule data allow us to postulate a free energy landscape for A2 unfolding (Fig. 3.7). Folding free energies determined by CD thermal denaturation indicate that native A2 (N) is stabilized by calcium (gray). Similar unfolding kinetics in the presence and absence of calcium dictate similar activation energies from N to the unfolding transition state (TS 1). As a result, calcium stabilizes TS 1 to the same extent as N. These similar energetics are a consequence of calcium occupying similar structural environments within TS 1 and N (20). Thus, our results indicate that TS 1 binds calcium with native-like coordination.

In the refolding direction, we assume that A2 does not bind calcium in the unfolded state (U), consistent with coordination of calcium by residues far apart in sequence, from residue 1498 to 1602. Going from calcium-free U to calcium-bound N, the significant binding energy between calcium and A2 measured by ITC precludes the calcium binding event from occurring during a transition state. Given that TS 1 binds calcium, such a calcium-free transition state in the refolding direction (TS 2) requires a calcium binding intermediate (I). Indeed, an unfolding intermediate has been previously described at 1,000 Hz with a 1.2 ms lifetime (9), too transient to be characterized by our data acquired at 500 Hz but consistent with an intermediate structure with high energy relative to N and U (Fig.3.7). Further insight into TS 2 is gleaned from the dependence of refolding on calcium. Our single molecule data demonstrate that calcium accelerates refolding. Thus, the rate limiting transition state from calcium-free U to calcium-bound N must also bind calcium, and cannot be TS 2. Instead, TS 1 functions as the kinetically relevant transition state by occupying a higher energy level than TS 2 in the refolding pathway. In our model, the disparate effects of calcium on unfolding and refolding kinetics are accounted for by an unfolding transition state, TS 1, that binds calcium with native-like coordination, and that is rate limiting in both unfolding and refolding pathways.

The known three-dimensional structure of A2 (Fig. 3.1) places some limits on the structure of calcium-binding TS 1. As previously introduced, calcium binds A2 at the junction between two topologically defined windings (Fig. 3.1A). Both windings begin near the center of the β-sheet but proceed in opposite directions. Winding 1 proceeds from the central β1-strand to the α3-helix, whereas winding 2 proceeds from the central β4-strand to the α6-helix (Fig. 3.1A). The calcium binding site includes Asp-1498 in the β1-strand, residues 1596, 1597, and 1600 in the α3-β4 loop, and Asn-1602 in the β4-strand (Fig. 3.1B). Similar unfolding kinetics implicate native-like coordination of calcium within the unfolding transition state, and locate the boundary between native-like and unfolded regions of A2 between the β4-strand and the C-terminus. This region includes the α4-less loop which, like the calcium binding site, might be important in regulating the kinetics of A2 refolding. Such a model is also

consistent with the idea that unpopping of the rigid C-terminal vicinal disulfide plug could be rate limiting for unfolding, as previously proposed (1).

A very recent study used optical tweezers to report that A2 unfolding requires higher forces in the presence of calcium, and primarily proceeds through a mechanically stable intermediate (11). Force extension behavior in this study was measured at 50 Hz and exhibited slow unfolding and refolding (on the order of seconds) with unfolding intermediates lasting 1-3 s. This behavior clearly differs from the highly cooperative unfolding and refolding (within ms) previously reported (9) and observed in our study, as well as the 1.2 ms lifetimes previously reported for A2 unfolding intermediates (9). Because we did not observe such slow phenomena in our thousands of characterized events, we think it is unlikely that A2 follows an alternative unfolding pathway, but rather attribute these discrepancies to different methods for suspending single molecules of A2 between beads. Whereas we attached DNA handles to both ends of A2, holding A2 approximately 260 nm away from each bead and preventing nonspecific interactions, the other study attached DNA at only one end of the A2 construct. Their A2 N-terminus contained a $(c\text{-}myc)_4$ tag that directly bound an anti-c-myc antibody-coated bead, placing A2 approximately 840 nm away from the DNA-bound bead but only 0-30 nm away from the $(c\text{-}myc)_4$ tag-bound bead (depending on whether the antibody coupled through its Fab or Fc region to the bead, which of the four c-myc tags the antibody (21) bound to, and fluctuations in the flexible c-myc tags and antibody at low force). DNA handles are not only much longer but also much stiffer than the c-myc tags. We speculate that direct physisorption of the A2 protein to the anti-c-myc bead could have occurred, and that sequential force discontinuities summing to the overall contour length of the polypeptide could have been convoluted with A2 unfolding and refolding. Robustness of the 28 measured events (11) was not tested by fits to biophysical models that predict exponential dependence of unfolding and refolding rates on applied force (17, 19). In contrast, our 1881 events were fit to such models, and we have reported estimates of k_0 and Δx for unfolding, and k_0 and κ for refolding.

VWF is a multidomain protein and interdomain interactions are likely important for regulating function. Thus, our study is limited in characterizing conformational dynamics within isolated VWF A2. However, studies on the A1-A2-A3 tridomain have demonstrated that force-induced A2 unfolding is required for cleavage in the presence of neighboring domains as well (22, 23), and that calcium mediated stabilization against thermal denaturation is exclusive to the A2 domain (11), affirming the relevance of understanding the unfolding dynamics within the isolated A2 domain.

ADAMTS13 circulates in the body as a constitutively active enzyme, with cleavage regulated by conformational changes within its substrate. Much attention on A2 conformational regulation has focused exclusively on unfolding (22, 23). However, given the slow kinetics of refolding, at equilibrium, VWF A2 is predicted to be fully unfolded at forces above 5 pN (Fig. 3.8), significantly lower than the 10 pN peak force estimated to be experienced by a 200-mer VWF at the highest shear stress measured in arteriolar flow (9). The concentration of ADAMTS13 in vivo is estimated at 6 nM (24), well below the estimated K_m of 160 nM (9) required for saturation binding to its unfolded substrate. Therefore, the time required for refolding regulates the availability of unfolded A2 for cleavage. Our data suggest that refolding plays a critical role in regulating VWF proteolysis and highlights the dynamic nature of A2 conformational change in dictating VWF function.

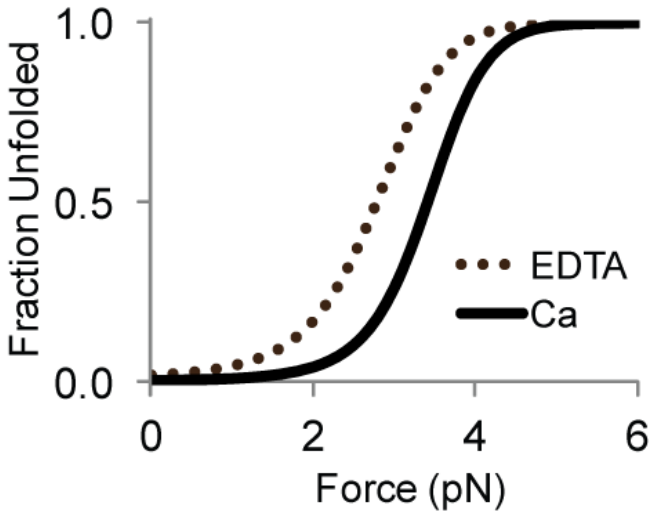

Figure 3.8. Fraction of unfolded A2 under applied force. The population of unfolded A2 under equilibrium predicted from the ratio of unfolding to refolding kinetics. In the absence of calcium, slowed refolding kinetics account for the increased fraction of unfolded A2. Our quantitative parameters predict that A2 is fully unfolded at forces above 5 pN.

Materials and methods

Circular Dichroism

Circular dichroism (CD) spectra were obtained on an Aviv 62 DS spectropolarimeter equipped with a Peltier temperature control unit (Aviv Associates, Lakewood, NJ). A2 protein (2 μM) in 20 mM Tris pH 7.50, 30 or 150 mM NaCl, and varying concentrations of EDTA or $CaCl_2$ was monitored within a 1.0 cm pathlength quartz cuvette with a magnetic stirrer. Baseline spectra of the folded and unfolded states were obtained at 4°C and 90°C, respectively, with 5 accumulations scanned from 260 to 195 nm at 1.0 nm intervals. Thermal denaturation was monitored at 222 nm from 4°C to 90°C at 1°C intervals, equilibrating for 2 minutes at each temperature before signal averaging for 1 minute. Spectra shown are corrected for background contribution of buffer. Thermal unfolding curves were derived from linear fits to thermal denaturation signal before and after the unfolding transition. Single wavelength CD temperature melts were fit to a Gibbs-Helmholtz equation as described by Greenfield (15).

Isothermal Calorimetry

Isothermal calorimetry was conducted on an iTC_{200} (Microcal, Piscataway, NJ) in a 200 μL reaction cell loaded with 140 μM protein at 25°C. To ensure complete removal of calcium, protein was dialyzed for 3 days against 5 mM EDTA, which was then removed via gel filtration on a Superdex 75 10/300 column (GE Lifesciences) immediately before the experiment. Titration was performed using 20 x 2 μL injections of 1.4 mM $CaCl_2$ in the same buffer (20 mM Tris, pH 7.5; 30 mM NaCl) at 180 s intervals, stirring at 1000 rpm. Binding isotherms were analyzed using the Microcal Origin version 7 software package and fit to a single site binding model.

Protein Expression and Purification

VWF A2 domain was prepared as previously described (9).

Single Molecule Sample Preparation

802 base pair DNA handles were PCR-amplified using forward primers with a 5'thiol group and reverse primers with either 5'biotin or 5'digoxigenin, and activated with 2,2'-dithio-dipyridine (DTDP) as described previously (9). For protein-DNA coupling, 50 μL of 12 μM of protein was reduced with 1 mM DTT for 1 hour at room temperature, followed by three sequential passages through 0.5 mL Zeba desalting columns (Pierce). Freshly reduced A2 (5 μM) was reacted with 3 μM DTDP activated handles in 20 μL 0.2 M sodium acetate, pH 5; 1 M NaCl, 1 mM EDTA. Reaction components were quickly mixed before incubating under argon in a 1.5 mL eppendorf for 16 hours at room temperature. In our hands, coupling was tricky and highly sensitive to DNA : protein ratios. Due to small volumes and rapid oxidation, precise concentrations were difficult to predict and thus coupling was performed in parallel across a range of protein:DNA ratios (Fig. 3.9B). Different handle preparations varied in coupling efficiency and the preparations were selected as described below and used for experiments. Coupling efficiency was assayed by running reaction products on 4-20% polyacrylamide gels. Ethidium bromide staining reported shifts in DNA handles upon successful coupling to A2, which was specifically verified via western blot analysis on the same gel (Fig. 3.9A). As final verification, constructs were tested on single molecule optical tweezers. For constructs with poor coupling efficiency, only DNA handle dimers or nonspecific extension lengths were observed with great effort. Successful coupling yielded constructs with reliable observations of single A2 unfolding events (>50% of tethers). Verified DNA/protein coupled constructs were aliquoted and stored at -80^{o}C.

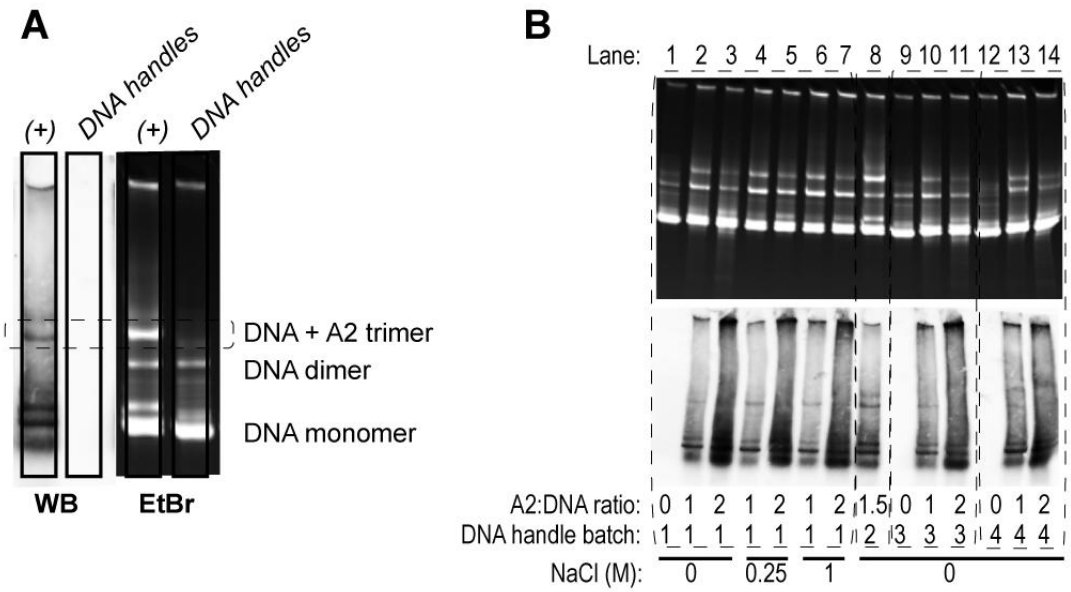

Figure 3.9. Coupling of vWF A2 to DNA handles. (A) Trimolecular construct verified by running the reaction on a 4-20% polyacrylamide gel and staining for DNA and vWF A2 in parallel. Following ethidium bromide (EtBr) staining, the same gel was subjected to Western blotting (WB) against the A2 histidine tag. (B) Full view of gels highlighted in A. Coupling efficiency, assessed via the presence of a trimolecular construct, was sensitive to DNA/protein ratio. Both too much protein (lane 2) and too much DNA (lane 3) resulted in poor yields of the trimolecular construct. Coupling efficiency varied with DNA handle preparations (four batches shown) and did not seem to be affected by NaCl concentrations (lanes 1-7, black bar). The best coupling (lane 8), visualized by the presence of a trimolecular construct, translated to reliable observations of unfolding events on single molecular optical tweezers.

Single Molecule Force Experiments

Polystyrene beads (4.2 μM, Spherotech) functionalized with anti-digoxigenin Fab (Roche) were incubated with 10 pM protein-DNA constructs for 30 min at room temperature (optimized for single tethers). Single beads were then trapped in the laser tweezers and brought close to a streptavidin-functionalized polystyrene bead (2.1 μM) suctioned onto the tip of a micropipette. Single tether formation was verified by overstretching the construct past 65 pN to confirm the signature force extension curve plateau corresponding to the S to B form DNA transition (25). The average tether lasted 80 cycles with force extension discontinuities observed in 75% of pulls. All pulls from each tether were used for analysis. The instrument used for optical trapping has been previously described (26). Experiments were conducted in 20 mM Tris pH 7.5, 150 mM NaCl, 0.02% Tween 20. Experiments were conducted with no added calcium (buffer confirmed as <20 μM Ca via a QuantiChrom Calcium Assay Kit; Bioassay Systems, Hayward, CA), with 5 mM $CaCl_2$, and with 1 mM EDTA.

Statistical Analysis

Errors are estimated errors based on χ^2 minimized fits using Origin 6.1 (OriginLab Corporation, Northampton, MA). Data were noted to be statistically similar by comparing the maximal spread of 95% confidence intervals.

Acknowledgments

The authors thank Dr. S.C. Blacklow for isothermal calorimetry and CD equipment and advice. This work was supported by NIH HL-48675 (TAS) and NIH/NIGMS T32 GM008313 (Molecular Biophysics Training Grant, A.J.X.). A.J.X. is an MD/PhD candidate at Harvard Medical School and this work is submitted in partial fulfillment of the requirement for the PhD.

Contribution

A.J.X. designed research, performed experiments, analyzed data, and wrote the paper. T.A.S. designed research and wrote the paper.

Conflict-of-interest disclosure:

The authors declare no competing financial interests.

References

1. Springer TA (2011) Biology and Physics of von Willebrand Factor Concatamers. *J Thromb Haemost* 9(Supplement 1):130-143.
2. Hoyer LW & Shainoff JR (1980) Factor VIII-related protein circulates in normal human plasma as high molecular weight multimers. *Blood* 55(6):1056-1059.
3. Schneider SW, *et al.* (2007) Shear-induced unfolding triggers adhesion of von Willebrand factor fibers. *Proc. Natl. Acad. Sci. U S A* 104:7899-7903.
4. Sadler JE (2005) New concepts in von Willebrand disease. *Annu Rev Med* 56:173-191.
5. Sadler JE, Moake JL, Miyata T, & George JN (2004) Recent advances in thrombotic thrombocytopenic purpura. *Hematology Am Soc Hematol Educ Program*:407-423.
6. Sadler JE (2008) Von Willebrand factor, ADAMTS13, and thrombotic thrombocytopenic purpura. *Blood* 112(1):11-18.
7. Zhang Q, Zhou Y-F, Zhang C-z, & Springer TA (2009) Structural specializations of A2, a force-sensing domain in the ultralarge vascular protein von Willebrand factor. *Proc. Natl. Acad. Sci. U S A* 106(23):9226-9231.
8. Dong JF, *et al.* (2002) ADAMTS-13 rapidly cleaves newly secreted ultralarge von Willebrand factor multimers on the endothelial surface under flowing conditions. *Blood* 100:4033-4039.
9. Zhang X, Halvorsen K, Zhang CZ, Wong WP, & Springer TA (2009) Mechanoenzymatic cleavage of the ultralarge vascular protein, von Willebrand Factor. *Science* 324:1330-1334.
10. Zhou M, *et al.* (2011) A novel calcium-binding site of von Willebrand factor A2 domain regulates its cleavage by ADAMTS13. *Blood* 117(17):4623-4631.
11. Jakobi AJ, Mashaghi A, Tans SJ, & Huizinga EG (2011) Calcium modulates force sensing by the von Willebrand factor A2 domain. *Nat Commun* 2:385.
12. Cruz MA, Whitelock J, & Dong JF (2003) Evaluation of ADAMTS-13 activity in plasma using recombinant von Willebrand Factor A2 domain polypeptide as substrate. *Thromb Haemost* 90(6):1204-1209.
13. Toumadje A, Alcorn SW, & Johnson WC, Jr. (1992) Extending CD spectra of proteins to 168 nm improves the analysis for secondary structures. *Anal Biochem* 200(2):321-331.
14. Boeckler FM, *et al.* (2008) Targeted rescue of a destabilized mutant of p53 by an in silico screened drug. *Proc. Natl. Acad. Sci. U S A* 105(30):10360-10365.
15. Greenfield NJ (2006) Using circular dichroism collected as a function of temperature to determine the thermodynamics of protein unfolding and binding interactions. *Nat Protoc* 1(6):2527-2535.
16. Ainavarapu SR, *et al.* (2007) Contour length and refolding rate of a small protein controlled by engineered disulfide bonds. *Biophys J* 92(1):225-233.
17. Dudko OK, Hummer G, & Szabo A (2006) Intrinsic rates and activation free energies from single-molecule pulling experiments. *Phys. Rev. Lett.* 96:108101-108104.
18. Evans E & Ritchie K (1997) Dynamic strength of molecular adhesion bonds. *Biophys. J.* 72:1541-1555.
19. Dudko OK, Hummer G, & Szabo A (2008) Theory, analysis, and interpretation of single-molecule force spectroscopy experiments. *Proc. Natl. Acad. Sci. U S A* 105(41):15755-15760.
20. Daggett V, Li A, Itzhaki LS, Otzen DE, & Fersht AR (1996) Structure of the transition state for folding of a protein derived from experiment and simulation. *J Mol Biol* 257(2):430-440.
21. Krauss N, *et al.* (2008) The structure of the anti-c-myc antibody 9E10 Fab fragment/epitope peptide complex reveals a novel binding mode dominated by the heavy chain hypervariable loops. *Proteins* 73(3):552-565.
22. Wu T, Lin J, Cruz MA, Dong JF, & Zhu C (2010) Force-induced cleavage of single VWF A1A2A3-tridomains by ADAMTS-13. *Blood* 115(2):370-378.
23. Ying J, Ling Y, Westfield LA, Sadler JE, & Shao JY (2010) Unfolding the A2 domain of von Willebrand factor with the optical trap. *Biophys J* 98(8):1685-1693.

24. Feys HB, *et al.* (2006) ADAMTS-13 plasma level determination uncovers antigen absence in acquired thrombotic thrombocytopenic purpura and ethnic differences *J. Thromb. Haemost.* 4:955-962.
25. Smith SB, Cui Y, & Bustamante C (1996) Overstretching B-DNA: The elastic response of individual double-stranded and single-stranded DNA molecules. *Science* 271:795-799.
26. Kim J, Zhang C, Zhang X, & Springer TA (2010) A mechanically stabilized receptor-ligand flex-bond important in the vasculature. *Nature* 466(7309):992-995.

Chapter IV:

Mechanism of A2 Domain Destabilization by Von Willebrand Disease Type 2A Mutations

Amy J. Xu and Timothy A. Springer

Abstract

von Willebrand Factor (VWF) thrombogenic activity is critically regulated through cleavage in the A2 domain by ADAMTS13, a proteolysis event that requires mechanical force to expose the scissile bond. Patients with von Willebrand Disease (VWD) type 2A present with increased bleeding due to mutations within A2 that enhance cleavage. In this study, we investigated the impact of three VWD type 2A mutations on A2 stability. Reversible thermal denaturation monitored using circular dichroism revealed that, under 1.25 mM Ca^{2+}, all three mutants reduced A2 thermal stability, shifting the melting temperature T_m 10-18 ^oC lower. Furthermore, R1597W, which resides within a calcium binding loop, diminished the shift in T_m by calcium from 11 ^oC more stable in wild-type A2, to only 2 ^oC. In contrast, M1528V retained calcium mediated stabilization, exhibiting a 15 ^oC shift in T_m, whereas E1638K required calcium for structural integrity, losing native structure even at 4^oC in the absence of calcium. Single molecule optical tweezers demonstrated that R1597W altered the force sensitivity of A2 unfolding and refolding in response to calcium. Whereas calcium enhanced refolding but not unfolding of wild-type A2, calcium slightly enhanced unfolding with little change in refolding kinetics for R1597W. These data demonstrate that VWD mutations destabilize VWF A2 and highlight structural features that govern the force sensitivity of VWF A2 unfolding and refolding.

Introduction

von Willebrand Factor (VWF) is a polymeric glycoprotein that critically mediates hemostasis through multivalent binding of integrins, clotting factor VIII, platelet glycoprotein Ib (GPIb), and collagen. Endothelial cells and platelets secrete VWF at sites of vascular injury as ultralong, disulfide-bonded concatamers (1) reaching >12 MDa in mass and >15 μm in length (2, 3). VWF functional activity correlates with size, with the largest VWF concatamers most avidly binding platelets and collagen in scaffolding a platelet plug.

VWF concatamer length, and hence thrombogenic activity, is regulated through cleavage by ADAMTS13 (a disintegrin and metalloprotease with a thrombospondin type 1 motif, member 13). In the absence of ADAMTS13 activity, extensive microvascular thromboses cause tissue ischemia and infarction, a life threatening condition known as thrombotic thrombocytopenic purpura (TTP). Conversely, increased VWF cleavage causes bleeding diatheses, and is known to result from mutations within the VWF gene that cluster within the VWF A2 cleavage domain.

ADAMTS13 circulates as a constitutively active protease whose activity is regulated by structural changes within A2. The ADAMTS13 cleavage site is buried within a central β4 strand that is inaccessible in the native state (Fig 4.1A). Hydrodynamic forces experienced by VWF concatamers in the vasculature apply tensile force to the N and C termini of A2, and single molecule studies have demonstrated that ADAMTS13 cleavage requires unfolding of the A2 domain to expose the scissile bond (4).

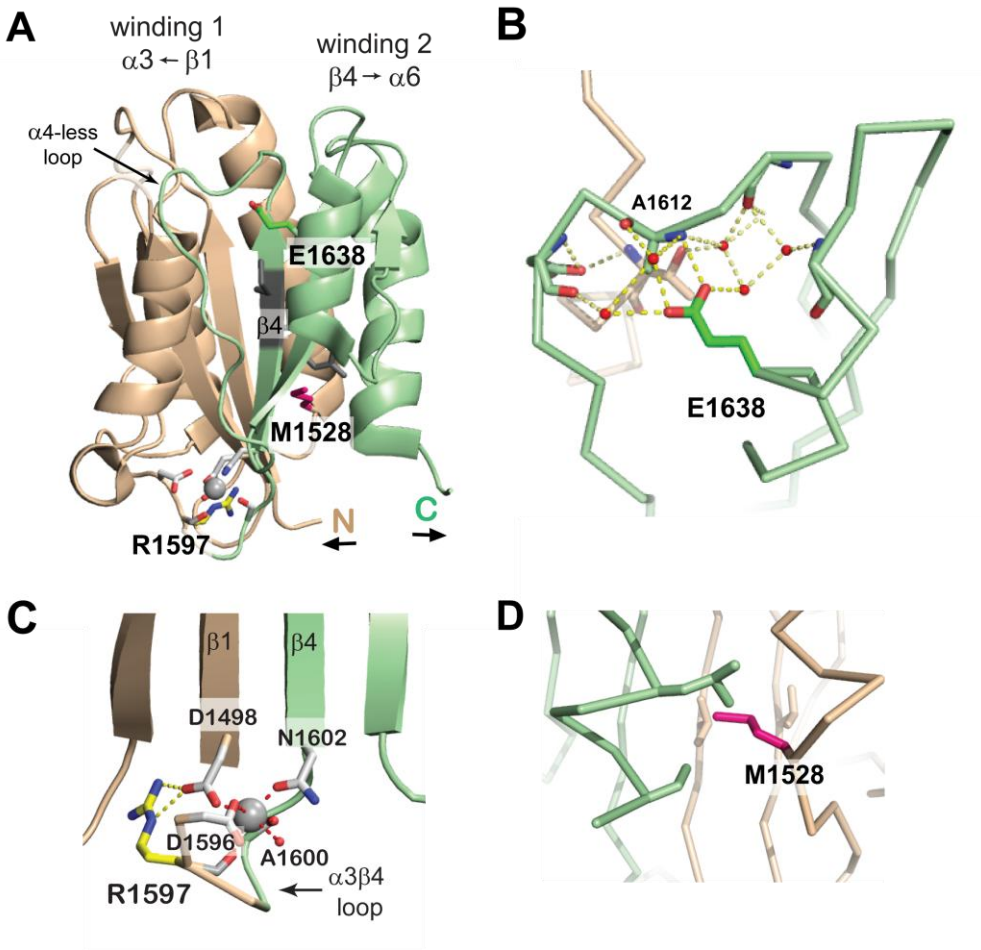

Fig 4.1. A2 structure. (A) The A2 domain is comprised of two windings. Winding 1 (wheat) proceeds from the N terminus and features a parallel arrangement of beta strands that confer mechanical resistance. Winding 2 (pale green) defines the C-terminal half of the domain and is predicted to be unraveled when tensile force is applied to the N and C temini (5), exposing the Y1605/M1606 scissile bond (grey) buried within the central β4 strand. A2 binds Ca^{2+} (silver sphere) within the α3β4 loop at the junction of these two windings. (B) E1638, within the α5 helix, forms a network of hydrogen bonds with buried water molecules and A1612 in the α4-less loop. (C) R1597, within the α3-β4 loop, directly coordinates calcium via its backbone carbonyl, and the arginine side chain forms a salt bridge with the sidechain of the Ca^{2+}-coordinating residue, Asp1498 within the β1 strand. (D) M1528 resides at the end of the α1 helix and is surrounded by hydrophobic residues. The structure shown is a chimera containing residues 1495-1578 and 1602-1672 of 3GXB (4) and residues 1579-1601 of 3PPV (6). Figure made with PYMOL.

VWF A2 is comprised of two topologically distinct windings (Fig 4.1A) and exhibits several structural features that enable sensitivity to force. Compared to neighboring A1 and A3 domains, A2 lacks a long-range disulfide bond to protect the domain against unfolding. Unfolding is predicted to proceed from the C terminus within winding 2 (pale green), where the alternating arrangement of beta strands and alpha helices favors stepwise unfolding. In contrast, winding 1 (wheat) features a parallel arrangement of beta strands that tightly locks the N terminus through hydrogen bond clamps within the A2 core. Molecular dynamic simulations also predict stepwise unfolding proceeding from the C terminus (5), and this model is consistent with biochemical characterizations of the minimal C-terminal portion required for maximal ADMTS13 cleavage (7). Within winding 2, A2 features an "α4-less" loop in place of an α4 helix that is thought to slow refolding to promote cleavage site accessibility (8). At the junction between winding 1 and winding 2, A2 also features a unique calcium binding site (silver) demonstrated to protect VWF against ADAMTS13 cleavage (6) and enhance refolding (9). These unique features within VWF A2 promote dynamic, force-dependent accessibility of the buried scissile bond.

Mutations within the VWF gene cause von Willebrand's disease (VWD), the most commonly inherited bleeding disorder in humans. Patients with type 2A VWD present with increased bleeding due to the decreased thrombogenicity of smaller VWF multimers (10). VWD type 2A mutations cluster within the A2 domain. Certain mutations have been described to impair VWF biosynthesis (Group 1) (11), whereas other mutations increase VWF proteolysis despite normal VWF multimer assembly and secretion (Group 2) (12, 13). Specifically, Group 2 mutations are thought to enhance cleavage by disrupting the stability of the folded A2 structure.

Previous studies have investigated the conformational stability of VWF A2 relative to neighboring domains. Consistent with the absence of a long-range disulfide bond, A2 was found to be more susceptible to chemical denaturation compared to A1 and A3 (14). In this study, we seek to understand the impact of VWD type 2A mutations on A2 conformational stability, and in particular, the dynamics of unfolding and refolding.

R1597W is by far the most common VWD type 2A mutation described in patients (15) and resides within the α3β4 calcium binding loop (Fig 4.1C). Though the backbone carbonyl directly binds calcium, R1597 forms a critical salt bridge with Asp1498, which resides within the β1 strand and is the only residue that coordinates calcium outside of the α3β4 loop. Previous studies using alanine substitution of calcium coordinating residues suggest that calcium stabilizes the A2 domain by neutralizing electrostatic repulsion between D1498 and D1596 (6, 16). We thus sought to understand the impact of R1597W on calcium mediated stabilization of A2.

We also explored the impact of two additional VWD type 2A mutations within the N and C terminal halves of the A2 domain. E1638K has been clinically described as a VWD type 2A mutant (17-19) and resides within the α5 helix, C-terminal to the scissile bond and within winding 2 (Fig 4.1B). M1528V has also been described to enhance A2 cleavage (13), and resides at the end of the α1 helix within winding 1 (Fig 4.1D).

Mutations were chosen to reflect disease prevalence as well as sample a range of structural environments. We first sought to characterize the impact of these mutations on conformational stability using thermodynamic denaturation. In parallel, we utilized single molecule optical tweezers to characterize the effect of VWD mutations on the force dependence of A2 conformational dynamics. The results demonstrate the impact of VWD 2A mutations on A2 stability, and provide insight into structural features regulating A2 unfolding and refolding dynamics that dictate ADAMTS13 cleavage.

Results

Thermal stability of VWD mutants under physiologic calcium concentrations

Circular dichroism (CD) spectra monitor changes in secondary structure. In the presence of calcium, all three VWD mutants exhibited spectra similar to wild-type A2 in Ca^{2+} at 4°C (Fig 4.2, black symbols). The spectra reflect the strong alpha helical content of the A2 domain, with double minima at 222 nm and 208 nm (20). Spectra remained stable for all constructs until at least 30°C, after which the native spectra lost alpha helical signature over a transition region spanning ~15°C until again becoming stable in a thermally denatured state (Fig 4.2, white symbols).

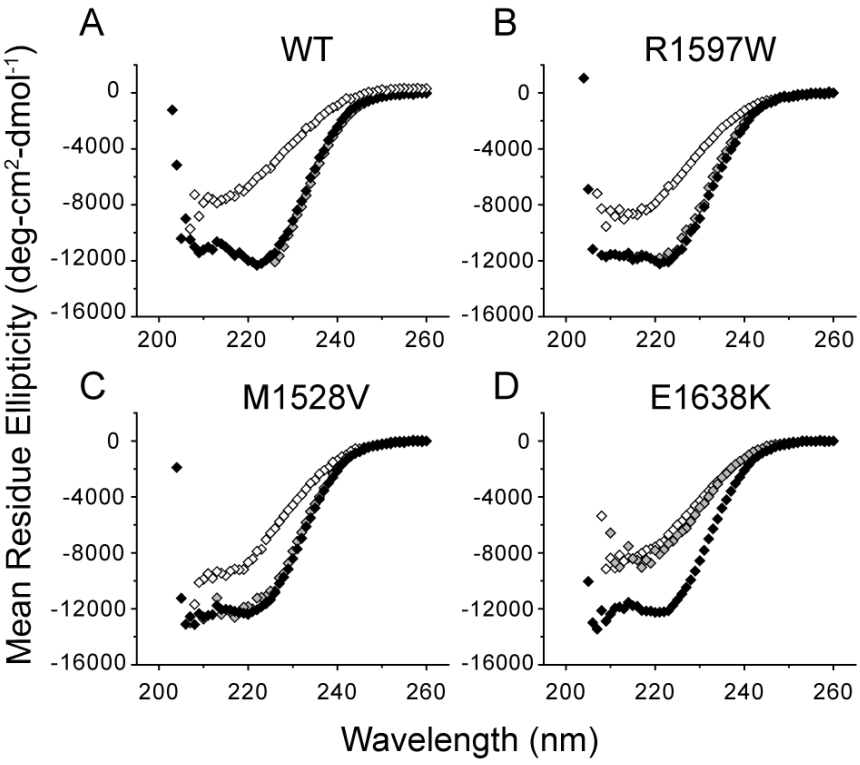

Fig 4.2. CD spectra of VWD A2. Under physiologic calcium concentrations, all VWD mutants exhibited similar native spectra compared to wild-type at 4°C (black). After thermal denaturation (white), the spectra lost alpha helical signature. Upon removal of calcium with 1 mM EDTA (grey), WT, R1597W, and M1528V retained native spectra whereas E1638K lost its native structure even at 4°C.

Thermal denaturation was quantitated at 222 nm, the wavelength of greatest contrast between native and denatured states (Fig 4.2), over a stepwise increase in temperature under equilibrium conditions (3 minutes per ^{o}C). Under physiologic 1.25 mM Ca^{2+}, all three VWD mutants were less stable against thermal denaturation compared to wild-type (Fig 4.3A). Whereas the half-point melting temperature T_m of wild-type A2 was 67.7 ^{o}C, M1528V, R1597W and E1638K exhibited decreased T_m temperatures of 57.9, 53.9, and 50.2 ^{o}C, respectively (Table 1).

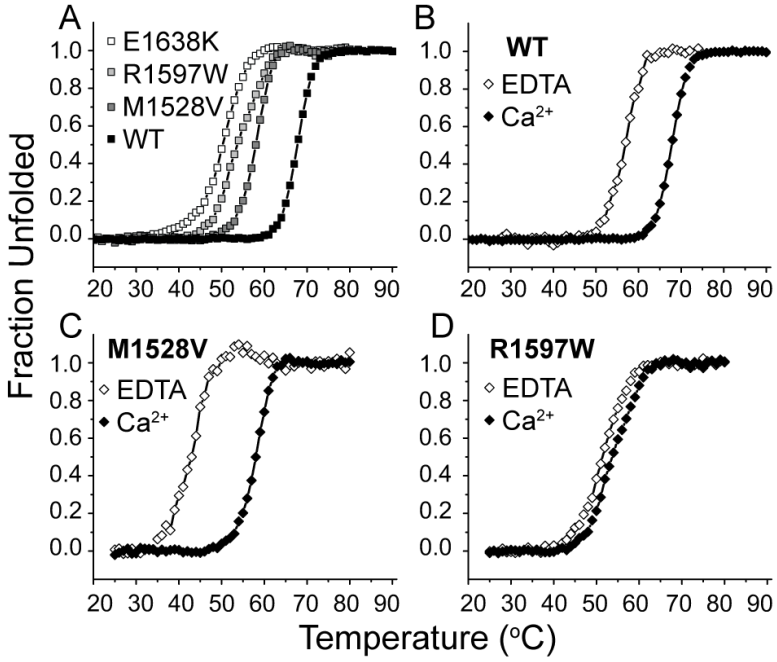

Fig 4.3. VWD A2 thermal denaturation. Thermal denaturation monitored at 222 nm over a stepwise increase in temperature at equilibrium (3 minutes per ^{o}C). (A) Under physiologic calcium concentrations (1.25 mM Ca^{2+}), all three mutants unfolded at lower temperatures compared to wild-type. (B) Wild-type A2 was stabilized against thermal denaturation in the presence of 1.25 mM Ca^{2+} compared to 1 mM EDTA. (C) R1597W diminished calcium stabilization. (D) M1528V was stabilized by calcium but at lower overall stabilities compared to wild-type.

Table 1. T_m values determined using CD.

	$T_{m,}$ ^oC			
	WT	R1597W	M1528V	E1638K
1.25 mM Ca	67.7 ± 0.1	53.9 ± 0.1	57.9 ± 0.1	50.2 ± 0.1
1 mM EDTA	56.7 ± 0.1	51.5 ± 0.1	42.6 ± 0.2	
Δ	11.0	2.4	15.3	

Calcium stabilization in VWD mutants

To monitor the effect of calcium on stabilizing A2 mutants, thermal denaturation was similarly monitored in the presence and absence of calcium (Fig 4.3B-D, Table 1). Wild-type A2 exhibited an 11 ^oC decrease in T_m in 1 mM EDTA compared to 1.25 mM Ca^{2+} (Fig 4.3B). The T_m of M1528V also exhibited a large decrease of 15 ^oC in the absence of calcium (Fig 4.3C, Table 1). E1638K, featuring the lowest T_m in the presence of calcium (Fig 4.3A), exhibited a sharp change in spectrum upon calcium removal at 4 ^oC. The E1638K 4 ^oC spectrum in 1 mM EDTA differed little from the 90 ^oC spectrum obtained in the presence of calcium (Fig 4.2D), and remained in this altered state throughout the stepwise temperature increase to 90^oC (data not shown). The large shift in T_m observed in M1528V, and loss of secondary structure observed in E1638K at 4^oC, suggest that, similar to its effect on wild-type A2, calcium plays an important role in stabilizing the native state of the M1528V and E1638K. In contrast, the R1597W mutant exhibited only a 2 ^oC decrease in T_m in the absence of calcium (Fig 4.3C, Table 1). This loss of calcium mediated stabilization strongly suggests that the R1597W mutation destabilizes the calcium-binding loop in which it resides.

Force-induced unfolding of R1597W

The effect of R1597W on force-dependent A2 unfolding and refolding was investigated using single molecule optical tweezers. VWF A2 was covalently linked through its N and C termini to DNA handles and suspended between two polystyrene beads, one anchored to the tip of a micropipette, and another trapped within the infrared dual beam laser focus of the optical tweezers (Fig 4.4A). Changes in light momentum reflected excursions of the bead from the center of the trap, *dx* (Fig 4.4A), and reported the force experienced by the protein-DNA tether with pN force sensitivity. Force extension profiles reported the stiffness of the single molecule construct, and A2 unfolding manifested as abrupt decreases in force (dashed circles, Fig 4.4B). Refolding was monitored by the presence or absence of unfolding in the subsequent pull (Fig 4.4B). Clamping at a low force between pulls provided time for A2 refolding.

Over a range of pulling rates, R1597W unfolding was similar to wild-type in displaying excellent agreement with full unfolding of VWF A2 (Fig 4.4C). The amount of extension over the range of forces where unfolding occurred (symbols, Fig 4.4C) was fit to the Worm-like Chain model of polymer elasticity (solid black line, Fig 4.4C). The fit yielded a persistence length, L_p, of 0.49 ± 0.02 nm. The contour length, or length of maximal extension, L_c, derived from the fit was 70.5 ± 1.18 nm. These results agree with previous measurements of wild-type A2 unfolding (dotted grey line, Fig 4.4C; L_p = 0.41 nm; L_c, = 75.6 nm) (9), and suggest full unfolding of R1597W A2 under all calcium conditions.

M1528V and E1638K coupling to DNA handles was verified via biochemical assay. However, repeated attempts were unsuccessful in finding multiple cycles of unfolding and refolding over many single molecule tethers with these mutant domains.

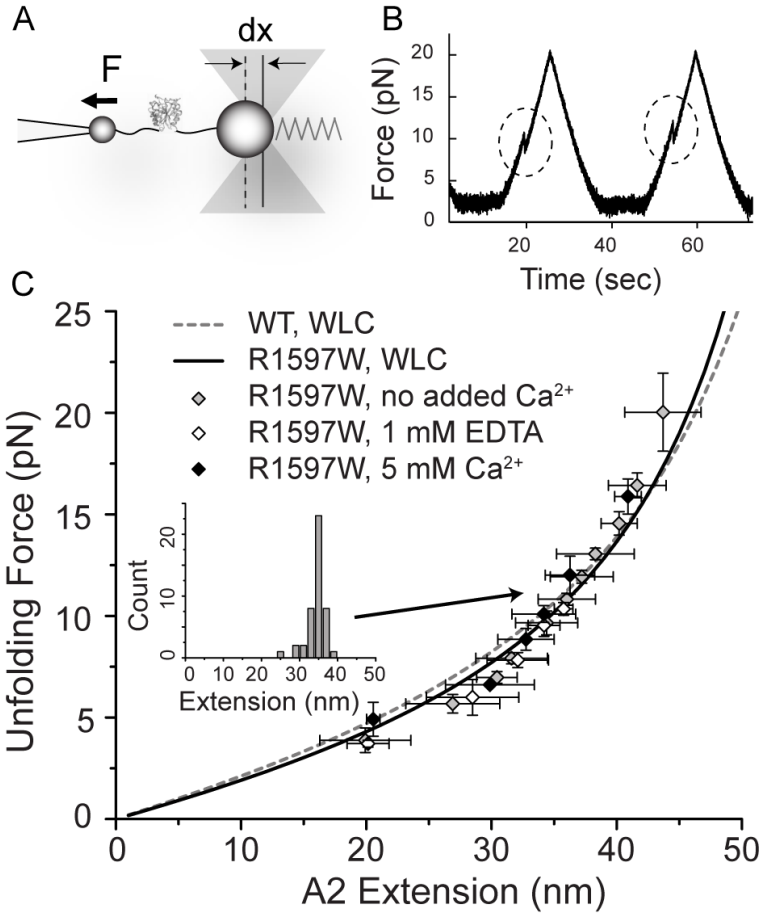

Fig 4.4. Monitoring protein unfolding using optical tweezers. (A) Experimental setup. Force spectroscopy performed on single A2 domains suspended between two polystyrene beads by DNA handles. Excursions of the bead from the center of the trap, dx, report the force experienced by the single molecule construct. (B) Representative unfolding events observed under 40 nm/s pulling and relaxation rates (corresponding to 0.5-2 pN/s force application rates) between 2 and 20 pN with 10 s pause at 2 pN to allow refolding. Force extension discontinuities are highlighted. (C) Worm Like Chain model fit to R1597W unfolding in the presence of no added Ca^{2+}, 5 mM Ca^{2+}, and 1 mM EDTA. Global fit for R1597W (black, solid) is compared with wild-type WLC fit (doted, grey) determined previously (21).

Calcium slightly stabilizes R1597W against unfolding

Unfolding kinetics were determined by examining the forces at which A2 unfolding was observed. R1597W (Fig 4.5A) and wild-type A2 (Fig 4.5B) exhibited a logarithmic dependence of unfolding force on loading rate, consistent with biophysical models of protein unfolding (22). Wild-type A2 exhibited similar unfolding kinetics in the presence and absence of calcium (within 20%, $p<0.05$, (9), Fig 4.5B). In contrast, R1597W exhibited a change in the response of unfolding to calcium, reflected in the force sensitivity parameter, σ, where $k=k_u^0 \exp(\sigma F/k_b T)$, and σ is given by the slope of the lines in Fig 4.5A. R1597W was more force resistant in the presence of calcium, as the folded state lifetimes decreased more slowly upon application of increasing force (Fig 4.5A, black line). In contrast, upon removal of calcium with 1 mM EDTA, R1597W exhibited a greater decrease in folded state lifetimes with increasing force (Fig 4.5A, dashed line). The extrapolated off-rate in the absence of force (k_u^0) was similar for R1597W in the presence and absence of force. Furthermore, the k_u^0 values for the R1597W mutant and wild-type in all conditions were indistinguishable (see k_u^0 values in Fig 4.5). Therefore, unfolding kinetics alone were not sufficient to account for the impact of R597W in destabilizing A2, observed as the decrease in T_m between R1597W wild-type A2 measured in the absence of force.

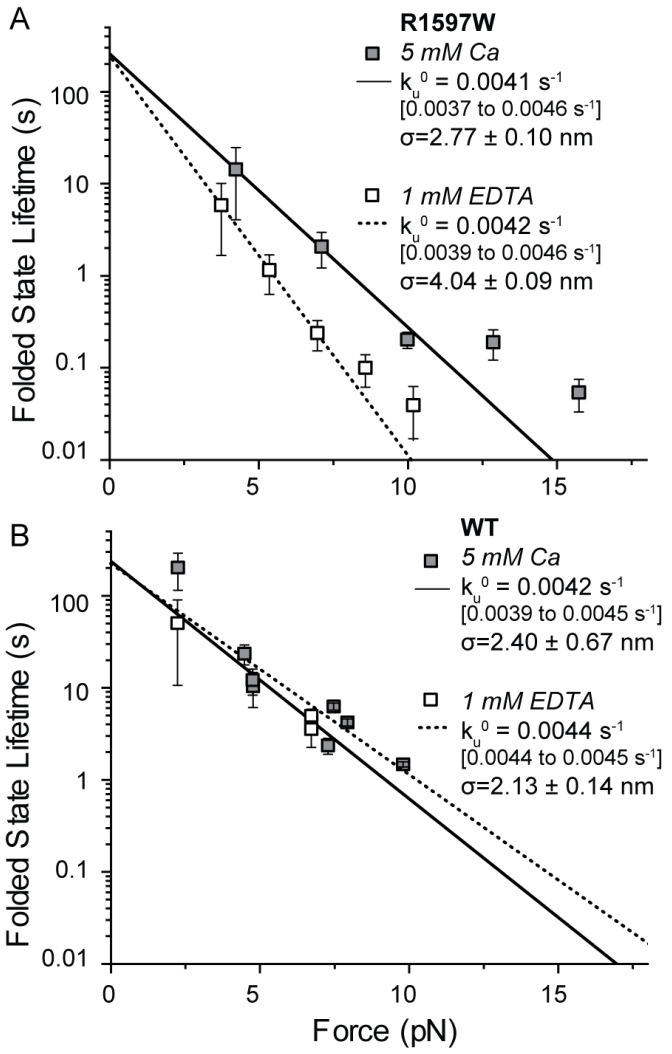

Fig 4.5. R1597W Unfolding. R1597W unfolding kinetics determined from the distribution of unfolding forces using the Hummer- Szabo-Dudko method (23). In contrast to wild-type A2, which fit similar unfolding kinetics in the presence and absence of Ca^{2+} (bottom), R1597W exhibited greater force resistance to unfolding (σ) in the presence of calcium (black) compared to EDTA (dotted).

R1597W refolding

To complement the measurements of R1597W unfolding, refolding kinetics were also measured over a range of forces. Compared to wild-type A2, R1597W exhibited significantly decreased probability of refolding in the presence of calcium (Fig 4.6A). In contrast to wild-type A2 refolding, which was significantly decreased in the absence compared to the presence of calcium, R1597W refolding remained similar upon calcium removal. Under both 5 mM Ca^{2+} and 1 mM EDTA, R1597W refolding was similar to wild-type A2 with calcium removed (Fig 4.6A).

Unfolded state lifetimes were determined from maximum likelihood estimations of refolding probabilities across different pause times over a range of forces. Each data point reflects the maximum likelihood estimation based on all refolding data obtained at a given minimum force. Theoretical fits were based on a single exponential dependence on the square of applied force, f^2, and the compliance of the unfolded state, κ (4) (Fig 4.6B). R1597W exhibited similar refolding kinetics in the presence and absence of calcium. At zero force, the intrinsic unfolded state lifetimes, τ_0, of R1597W were similar (7.2 and 9.2 s in the presence and absence of calcium, respectively, Fig 4.6B). R1597W refolding contrasted with wild-type A2, which exhibited enhanced refolding in the presence of calcium (τ_0 = 7.1 and 2.5 s in the presence and absence of calcium, respectively, Fig 4.6B). In both the presence and absence of calcium (dark gray and dashed gray, respectively), R1597W refolding was similar to wild-type A2 refolding with calcium removed (dotted black).

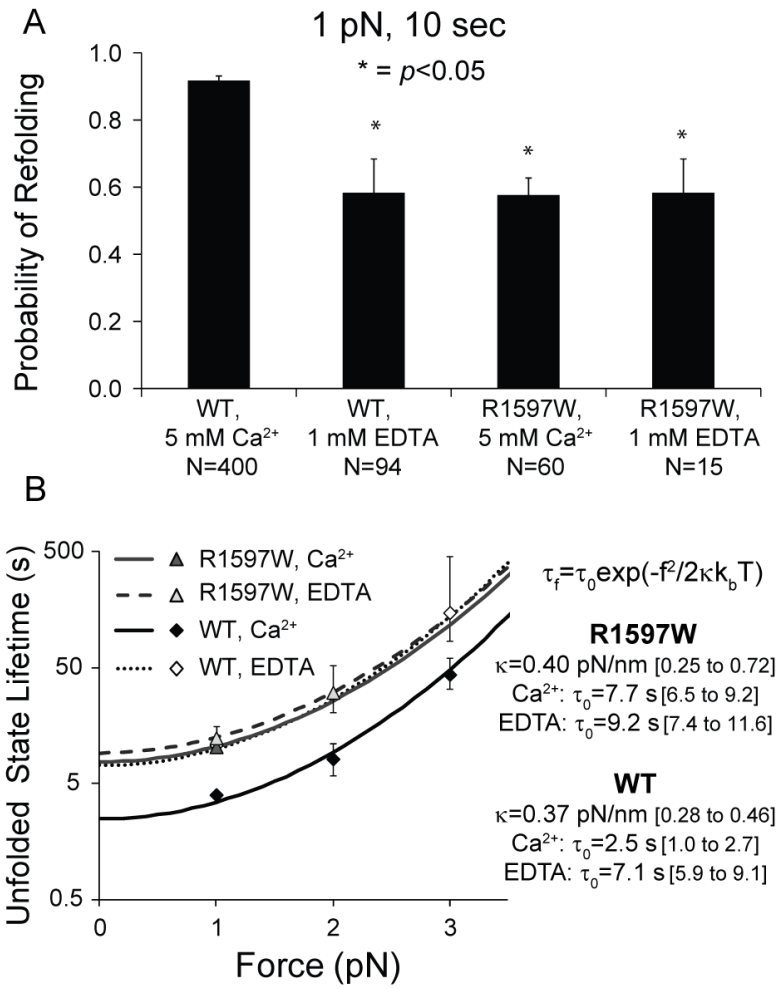

Fig 4.6. R1597W Refolding. A) Binary refolding statistics collected for 10 s pauses at 1 pN. In the presence of calcium, R1597W significantly decreased the probability of refolding compared to wild-type. R1597W refolding was similar in the presence and absence of calcium. Under both 5 mM Ca and 1 mM EDTA, R1597W refolding was significantly decreased compared to wild-type A2 in the presence of calcium, similar to wild-type A2 refolding in 1 mM EDTA. B) Predicted unfolded state lifetimes determined from maximum likelihood estimates of refolding probabilities obtained at different minimum pause forces for varying lengths of time. Theoretical fits based on an exponential dependence of refolding on the square of applied force (4). Whereas wild-type refolding was enhanced with 5 mM Ca^{2+} compared to 1 mM EDTA (dotted and solid black lines, respectively), little difference was observed between 5 mM Ca^{2+} and 1 mM EDTA in R1597W (solid and dashed grey lines, respectively).

Discussion

In this study, we investigated the mechanisms by which mutations in VWF A2 cause VWD type 2A using bulk measurements of thermodynamic denaturation combined with single molecule measurements of unfolding and refolding kinetics. Specifically, we demonstrated the impact of three VWD type 2A Group 2 mutations, R1597W, M1528V and E1638K, in destabilizing VWF A2. Under physiologic calcium concentrations, these mutants exhibited alpha-helical content similar to wild-type A2, suggesting that A2 structure remained intact prior to thermal denaturation. However, all three mutations exhibited decreased stability to thermal denaturation compared to wild-type A2, suggesting that these clinical mutations enhance ADAMTS13 proteolysis by destabilizing the A2 domain.

We further probed the impact of these VWD mutations on calcium mediated stabilization of VWF A2 by monitoring thermal denaturation in the presence and absence of calcium. M1528V and E1638K, outside of the calcium binding loop, retained stabilization by calcium binding. M1528V exhibited a 15.3 ^{o}C stabilization against thermal denaturation in the presence of calcium (Fig 4.3C) whereas E138K required calcium to stabilize the native structure at 4^{o}C (Fig 4.2D). M1528V resides within the more mechanically stable winding 1 that is predicted to remain folded and confer resistance against rupture. The methionine sidechain protrudes into a hydrophobic environment that is presumably destabilized upon substitution with the less bulky valine sidechain. M1528V retained calcium stabilization but at overall lower thermodynamic stabilities, consistent with the mutation decreasing the force resistance of the domain but not disrupting the native state. In contrast, the Glu^{1638} side chain resides within the less force resistant winding 2, and forms multiple H bonds with the backbone of the α4-less loop and a network of buried water molecules (Fig 4.1B). The loss of E1638K native structure upon removal of calcium demonstrates that both the α4less network of hydrogen bonds and calcium binding loop critically stabilize the folded state.

In contrast, to wild-type A2 and mutations residing outside the calcium binding loop, R1597W, exhibited only a 2 ^{o}C T_m shift in the presence of calcium, demonstrating significant disruption of calcium mediated stabilization. Residing within the calcium binding loop, Arg1597's backbone carbonyl directly coordinates calcium while the sidechain forms a salt bridge with Asp 1498, the only residue outside of the α3β4 loop involved in A2 calcium coordination (Fig 4.1C). The diminished calcium stabilization observed with R1597W under thermal denaturation (Fig 4.3C) is likely due to loss of Asp1498 stabilization. R1597W and R1597Q are the two most frequently reported VWD 2A mutations and account for 65% of all VWD type 2A mutations described in the ISTH database (15). The disruption of calcium-mediated stabilization in R1597W thus highlights the importance of calcium stabilization for VWF function.

Previous studies have demonstrated that calcium modulates wild-type A2 stability and ADAMTS13 sensitivity. VWF A2 binds calcium with μM affinity (9) and calcium binding has been shown to protect the domain against cleavage (6, 16) and enhance A2 refolding (9). The mechanism of calcium mediated stabilization has also been studied through alanine substitutions of calcium coordinating residues (6, 16). Consistent with loss of calcium binding, D1596A and N1602 mutations abolished calcium mediated increases in A2 thermal stability. In both the presence and absence of calcium, N1602A destabilized thermal stability similar to calcium-free wild-type A2. In contrast, D1596A paradoxically increased A2 thermal stability in the absence of calcium, presumably due to the neutralization of electrostatic repulsion between D1498, within the β1 strand, and D1596, within the α3β4 loop. These characterizations of thermal stability correlate with ADAMTS13 sensitivity, suggesting that calcium mediates increased A2 stability and cleavage resistance by neutralizing electrostatic repulsion within the calcium-binding pocket (16).

To further probe the mechanism of calcium-mediated stabilization, we explored R1597W unfolding and refolding dynamics in the presence and absence of calcium using single molecule optical tweezers. Similar to wild-type A2, R1597W extension lengths were consistent with full domain

unfolding under all calcium conditions (Fig 4.4C). The similar contour lengths preclude calcium binding in the unfolded state, especially since calcium binding involves residues far apart in sequence. Consistent with almost complete loss of calcium stabilization observed with thermal denaturation, there was little influence of calcium on R1597W refolding kinetics. Under both 5 mM Ca^{2+} and 1 mM EDTA, R1597W refolding kinetics were similar to those of calcium free wild-type A2. Thus, loss of calcium-dependent stabilization contributes to the decreased stability observed in the most frequently observed substitution in VWD type 2A, R1597W.

R1597W was also distinct from wild-type A2 in exhibiting different force-dependent unfolding kinetics in the presence and absence of calcium (Fig 4.5). In the absence of calcium, R1597W exhibited a greater susceptibility to unfolding upon application of force. This difference manifested as an increase in σ, reflecting the sensitivity to force, or distance to the transition state, indicating that the mutant is more easily deformed. The change in A2 compliance may result from loss of the stabilizing interaction between the sidechains of Arg-1597 and Asp-1498 in the wild-type structure, or perturbation by Trp-1597 of the unfolding pathway in the mutant structure. The expected unfolded fractions under force equilibrium demonstrate how this change in force sensitivity affects overall stability (Fig 4.7).

The discrepancy between calcium affecting R1597W but not wild-type unfolding suggests differences between R1597W and wild-type in the rate limiting transition state for unfolding. Several studies implicate an intermediate state in the VWF A2 unfolding pathway (4, 9, 16) and molecular dynamic simulations predict an unfolding intermediate after the unraveling of $\alpha 6$, $\beta 6$ and $\alpha 5$ (5). The contour lengths of unfolded R1597W and wild-type A2 are essentially identical, and consistent with full unfolding of A2. The difference in the role of calcium between wild-type and R1597W unfolding suggests that R1597W differentially affects calcium binding in the native and intermediate states. Specifically, the ability of calcium to stabilize R1597W, but not wild-type A2, against unfolding, suggests that R1597W is more disruptive to calcium binding in the intermediate state than the native structure.

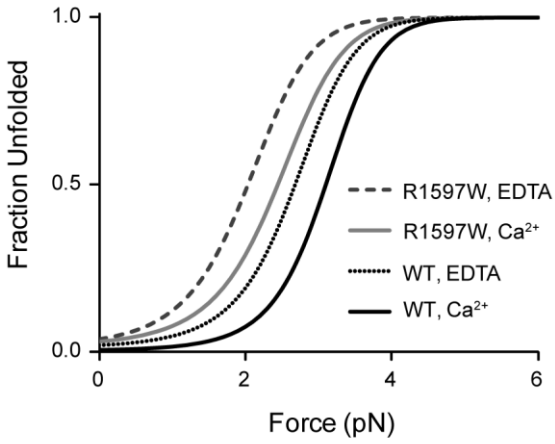

Figure 4.7. Fraction of unfolded A2 under applied force.

The population of unfolded A2 under equilibrium predicted from the ratio of unfolding to refolding kinetics. Under physiologic calcium conditions, our quantitative parameters predict that A2 is fully unfolded at forces above 3 pN for R1597W (solid gray), and 5 pN for wild-type A2 (solid black).

The three VWD mutations studied here each point out important features of the A2 domain that help specialize it for force-dependent size regulation of VWF. The α3β4 loop bearing the calcium binding site appears to be critical in regulating the force sensitivity of A2 unfolding. Loss of calcium stabilization accounts for the destabilization observed in the most commonly described site of VWD type 2A mutations, R1597. Under physiologic calcium conditions, R1597W exhibits similar unfolding kinetics compared to wild-type. The main difference is that R1597W refolding resembles the calcium free wild-type phenotype, underscoring the importance of refolding kinetics to VWF function. The importance of refolding is also highlighted by A2's remarkable absence of a homologous α4 loop, a structural specialization hypothesized to slow refolding. E1638 forms multiple hydrogen bonds with A1612 and buried water molecules within the α4-less loop. Upon E1638K substitution, the α4-less loop loses a stabilizing contact with the α5 helix (Fig 4.1B). The low stability of E1638K, especially upon removal of calcium, highlights the destabilizing structural feature that the α4-less loop provides the A2 domain. The force resistance conferred by the N terminal winding 1 is highlighted by the overall decrease in thermal stability, but not loss of native structure, observed in M1528V. The impact of these VWD type 2A mutations on A2 stability highlights the structural features of calcium binding, the α4-less loop, and the mechanically stabilized N-terminal beta sheets that render VWF A2 remarkably sensitive to hydrodynamic forces experienced in the vasculature.

Materials and methods

Circular Dichroism

Circular dichroism (CD) spectra were obtained on an Aviv 62 DS spectropolarimeter equipped with a Peltier temperature control unit (Aviv Associates, Lakewood, NJ). A2 protein (2 μM) in 20 mM Tris pH 7.50, 30 mM NaCl, and either 1 mM EDTA or 1.25 mM $CaCl_2$ was monitored within a 1.0 cm pathlength quartz cuvette with a magnetic stirrer. Baseline spectra of the folded and unfolded states were obtained at 4°C and 90°C, respectively, with 5 accumulations scanned from 260 to 195 nm at 1.0 nm intervals. Thermal denaturation was monitored at 222 nm at 1°C intervals, equilibrating for 2 minutes at each temperature before signal averaging for 1 minute. Spectra shown are corrected for background contribution of buffer. Thermal unfolding curves were derived from linear fits to thermal denaturation signal before and after the unfolding transition. Single wavelength CD temperature melts were fit to a Gibbs-Helmholtz equation as described by Greenfield (24).

Protein Expression and Purification

VWF A2 was prepared as previously described (4). VWD mutations were introduced using overlap PCR.

Single Molecule Force Experiments

Single molecule constructs (Fig 4.8) and optical tweezers experiments were prepared as previously described (9).

Statistical Analysis

Errors were estimated by χ^2 minimized fits using Origin 6.1 (OriginLab Corporation, Northampton, MA).

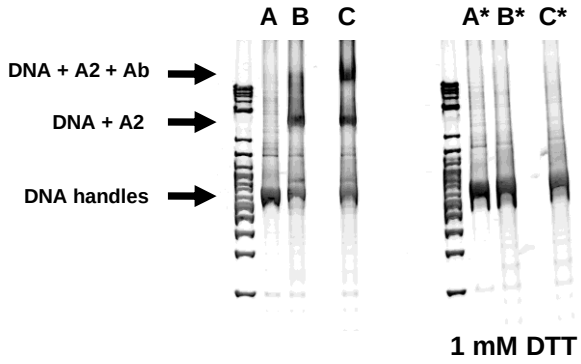

Figure 4.8. R1597W DNA Coupling.

DNA coupling. 4-20% TBE gel stained for DNA using EtBr. (*A) DNA handles only; (B) DNA handles + R1597W.* Gel shift due to coupling of A2 domain; (*C) DNA+R1597W+aA2 antibody.* Gel shift upon A2 antibody binding to A2 domain; *(*)* Both interactions abolished under reducing conditions (1 mM DTT).

Acknowledgments:

The authors thank Dr. S.C. Blacklow for CD equipment and advice, and Dr. W.P. Wong for useful discussion about statistical analysis. This work was supported by NIH HL-48675 (TAS) and NIH/NIGMS T32 GM008313 (Molecular Biophysics Training Grant, A.J.X.). A.J.X. is an MD/PhD candidate at Harvard Medical School and this work is submitted in partial fulfillment of the requirement for the PhD.

Contribution:

A.J.X. designed research, performed experiments, analyzed data, and wrote the paper. T.A.S. designed research and wrote the paper.

Conflict-of-interest disclosure:

The authors declare no competing financial interests.

References

1. Springer TA (2011) Biology and Physics of von Willebrand Factor Concatamers. *J Thromb Haemost* 9(Supplement 1):130-143.
2. Hoyer LW & Shainoff JR (1980) Factor VIII-related protein circulates in normal human plasma as high molecular weight multimers. *Blood* 55(6):1056-1059.
3. Schneider SW, *et al.* (2007) Shear-induced unfolding triggers adhesion of von Willebrand factor fibers. *Proc. Natl. Acad. Sci. U S A* 104:7899-7903.
4. Zhang X, Halvorsen K, Zhang CZ, Wong WP, & Springer TA (2009) Mechanoenzymatic cleavage of the ultralarge vascular protein, von Willebrand Factor. *Science* 324:1330-1334.
5. Baldauf C, *et al.* (2009) Shear-induced unfolding activates von Willebrand factor A2 domain for proteolysis. *J Thromb Haemost* 7(12):2096-2105.
6. Zhou M, *et al.* (2011) A novel calcium-binding site of von Willebrand factor A2 domain regulates its cleavage by ADAMTS13. *Blood* 117(17):4623-4631.
7. Kokame K, Matsumoto M, Fujimura Y, & Miyata T (2004) VWF73, a region from D1596 to R1668 of von Willebrand factor, provides a minimal substrate for ADAMTS-13. *Blood* 103(2):607-612.
8. Zhang Q, Zhou Y-F, Zhang C-z, & Springer TA (2009) Structural specializations of A2, a force-sensing domain in the ultralarge vascular protein von Willebrand factor. *Proc. Natl. Acad. Sci. U S A* 106(23):9226-9231.
9. Xu AJ and Springer TA. Calcium stabilizes the von Willebrand factor A2 domain by promoting refolding. *Proc Natl Acad Sci U S A* 109(10):3742-3747.
10. Sadler JE (2005) New concepts in von Willebrand disease. *Annu Rev Med* 56:173-191.
11. Lyons SE, Bruck ME, Bowie EJ, & Ginsburg D (1992) Impaired intracellular transport produced by a subset of type IIA von Willebrand disease mutations. *J Biol Chem* 267(7):4424-4430.
12. Sadler JE, *et al.* (2006) Update on the pathophysiology and classification of von Willebrand disease: a report of the Subcommittee on von Willebrand Factor. *J Thromb Haemost* 4(10):2103-2114.
13. Hassenpflug WA, *et al.* (2006) Impact of mutations in the von Willebrand factor A2 domain on ADAMTS13-dependent proteolysis. *Blood* 107(6):2339-2345.
14. Auton M, Cruz MA, & Moake J (2007) Conformational stability and domain unfolding of the Von Willebrand factor A domains. *J Mol Biol* 366(3):986-1000.
15. Hampshire D (2009) ISTH-SSC VWF Online Database.
16. Jakobi AJ, Mashaghi A, Tans SJ, & Huizinga EG (2011) Calcium modulates force sensing by the von Willebrand factor A2 domain. *Nat Commun* 2:385.
17. Lavergne JM, *et al.* (1991) Carrier detection and prenatal diagnosis in 98 families of haemophilia A by linkage analysis and direct detection of mutations. *Blood Coagul Fibrinolysis* 2(2):293-301.
18. Christophe O, *et al.* (1994) Influence of mutations and size of multimers in type II von Willebrand disease upon the function of von Willebrand factor. *Blood* 83(12):3553-3561.
19. Ribba AS, Voorberg J, Meyer D, Pannekoek H, & Pietu G (1992) Characterization of recombinant von Willebrand factor corresponding to mutations in type IIA and type IIB von Willebrand disease. *J Biol Chem* 267(32):23209-23215.
20. Toumadje A, Alcorn SW, & Johnson WC, Jr. (1992) Extending CD spectra of proteins to 168 nm improves the analysis for secondary structures. *Anal Biochem* 200(2):321-331.
21. Xu A & Springer TA (2011) Calcium Stabilizes the von Willebrand Factor A2 Domain by Promoting Folding.
22. Evans E & Ritchie K (1997) Dynamic strength of molecular adhesion bonds. *Biophys. J.* 72:1541-1555.
23. Dudko OK, Hummer G, & Szabo A (2008) Theory, analysis, and interpretation of single-molecule force spectroscopy experiments. *Proc. Natl. Acad. Sci. U S A* 105(41):15755-15760.

24. Greenfield NJ (2006) Using circular dichroism collected as a function of temperature to determine the thermodynamics of protein unfolding and binding interactions. *Nat Protoc* 1(6):2527-2535.

Summary and Future Directions

VWF is a fascinating protein that plays critical roles in hemostasis and is remarkably sensitive to hydrodynamic forces within the vasculature. This thesis focused on the structural specializations that render the A2 cleavage domain sensitive to force. We used bulk thermodynamic assays to demonstrate that VWF binds calcium at physiologic calcium concentrations and that calcium stabilizes VWF A2 against thermal denaturation. Single Molecule Optical Tweezers were employed to demonstrate that calcium stabilizes VWF A2 by accelerating refolding. These findings emphasize the importance of refolding to dynamically regulating VWF accessibility to proteolysis by ADAMTS13.

VWF A2 stability was also studied in the context of patient mutations known to cause the bleeding diathesis of VWD. Three VWD 2A mutations were studied, all of which destabilized A2 against thermal denaturation under physiologic calcium concentrations. The relevance of calcium binding to physiology was emphasized by demonstrating that R1597W, the most commonly reported VWD 2A mutation, diminishes calcium mediated stabilization. In contrast, other VWD 2A mutations outside the calcium binding site maintained stabilization by calcium. On optical tweezers, calcium slightly stabilized R1597W against unfolding but did not affect R1597W refolding. The similarity of R1597W refolding to calcium-free wild-type A2 refolding highlights the critical role of refolding, not just unfolding, for regulating VWF cleavage by ADAMTS13. The difference in the role of calcium between wild-type and R1597W unfolding suggests that R1597W differentially affects calcium binding in the native and intermediate state. In addition to monitoring mechanical unfolding and folding kinetics using single molecule optical tweezers, unfolding and refolding in response to chemical dentaurants such as urea or guanidine hydrochloride would also be interesting to minitor using stopped flow fluorescence of circular dichroism. Such structural insights may prove useful in designing modulators of VWF function.

It will be interesting to directly assess VWF cleavage kinetics under force using multiplexed single molecule assays. Though single molecule optical tweezers offer precise control over the

mechanical force applied to each molecule, they are intractable for obtaining bulk statistics to characterize enzyme kinetics. Systems optimized for massively parallel single molecule observations, such as Centrifugal Force Microscopy (CFM), allow for the numerics of ensemble measurements while retaining single molecule mechanical control. It will be interesting to study VWF mechanoregulation using CFM to characterize the kinetics of ADAMTS13 cleavage over a range of forces. Below the threshold for complete unfolding of the A2 domain, we expect ADAMTS13 cleavage to increase with greater force. Furthermore, we expect VWD mutants to be cleaved at lower forces. Quantitative analysis of single molecule cleavage kinetics will provide a better understanding of how pathology arises from disordered VWF A2 mechanoregulation.

The studies in this thesis were isolated to the A2 domain. Interdomain interactions between A2 and neighboring domains likely play a role in regulating A2 function, and the inclusion of these interactions will enhance the understanding of A2 function. In addition, ADAMTS13 has binding sites outside of the A2 domain which may be important in the force regulation of A2 cleavage. It will be intriguing to directly test the role of elongational force in activating VWF function, and confirm these force regulatory mechanisms *in vivo*.

VWF is a large, concatameric polymer exposed to a range of hydrodynamic forces in the vasculature. In addition to providing a better understanding of VWD pathophysiology and A2 unfolding and refolding dynamics, these studies enhance the understanding of how mechanical forces experienced within the vasculature regulate processes of hemostasis and thrombosis. Characterizing the force sensitivity of the VWF A2 domain provides an intriguing glimpse into the power of mechanical force in regulating biological processes.